JGR Atmospheres

RESEARCH ARTICLE
10.1029/2019JD031699

Environmental Controls on Tropical Sea Breeze Convection and Resulting Aerosol Redistribution

J. M. Park[1], S. C. van den Heever[1], A. L. Igel[2], L. D. Grant[1], J. S. Johnson[3], S. M. Saleeby[1], S. D. Miller[4], and J. S. Reid[5]

[1]Department of Atmospheric Science, Colorado State University, Fort Collins, CO, USA, [2]Department of Land, Air and Water Resources, University of California, Davis, CA, USA, [3]Institute for Climate and Atmospheric and Science, University of Leeds, Leeds, UK, [4]Cooperative Institute for Research in the Atmosphere, Colorado State University, Fort Collins, CO, USA, [5]Naval Research Laboratory, Monterey, CA, USA

Key Points:
- Environmental parameters controlling the characteristics of moist tropical sea breeze convection and aerosol transport are identified
- Wind speed and soil saturation fraction are the primary controls of the inland propagation characteristics of the sea breeze front
- Sea breeze convective intensity is dominated by inversion strength (boundary layer potential temperature) for shallower (deeper) clouds

Correspondence to:
J. M. Park,
jungminp@colostate.edu

Citation:
Park, J. M., van den Heever, S. C., Igel, A. L., Grant, L. D., Johnson, J. S., Saleeby, S. M., et al. (2020). Environmental controls on tropical sea breeze convection and resulting aerosol redistribution. *Journal of Geophysical Research: Atmospheres*, *125*, e2019JD031699. https://doi.org/10.1029/2019JD031699

Received 19 SEP 2019
Accepted 17 FEB 2020
Accepted article online 21 FEB 2020

Abstract Sea breeze fronts propagate inland from the coastline, driving convective initiation and aerosol redistribution. Forecasting sea breezes is challenging due to uncertainties in the initial conditions, as well as the covariance and interaction of various meteorological and surface parameters. Using the Regional Atmospheric Modeling System coupled to an interactive land-surface model, we conduct an ensemble of 130 idealized cloud-resolving simulations by simultaneously perturbing six atmospheric and four surface parameters describing the initial conditions. To identify the key parameters impacting the inland characteristics and the intensity of the sea breeze convection in a tropical rainforest, we apply statistical emulation and variance-based sensitivity analysis techniques. This study extends a previous study which explored the impacts of various parameters on sea breeze characteristics in arid environments devoid of moist convection. Wind speed is identified as the main contributor to the inland extent, similar to the arid environment study. However, the relative impacts of surface properties on the inland extent are less significant in the moist environment where land-surface heating can be suppressed via moist convective processes and vegetation-atmosphere interactions. Two sea breeze-initiated convection regimes are also identified: shallow and deep. Over the shallow regime, where convective available potential energy is limited, the inversion layer strength is the primary control of the convective intensity. Over the deep regime, boundary layer temperature exerts a robust control over the convective available potential energy and hence the convective intensity. The potential vertical redistribution of aerosols is closely related to the convective intensity.

1. Introduction

Along the coastlines, the discontinuities between radiative and thermodynamic properties of the land and the ocean regions lead to the land-sea breeze circulation (Crosman & Horel, 2010; Miller et al., 2003; Simpson, 1994). During the day, differential heating over land and ocean surfaces creates an inland-directed pressure gradient force. In response, a relatively colder, moister, and more stable marine air mass advances inland, with compensating offshore flow aloft. On the landward side, the convergence at the leading edge of the circulation induces upward motion, which supports convective cloud formation by lifting the low-level air parcels to the level of free convection.

The sea breeze can affect a wide range of human activities along the coastlines, including recreation, agriculture, transportation, naval activities, wind energy use, and industry. Given that nearly half of the world's population resides within 150 km of the coastline and that this coastal population is expected to continue increasing (United Nations Atlas of the Oceans http://www.oceansatlas.org), it is important to provide reliable forecasts of sea breeze convection and associated coastal air quality. Observations indicate that the horizontal extent of sea breezes varies from a few kilometers to several hundred kilometers inland (Clarke, 1983; Muppa et al., 2012; Physick & Smith, 1985) and from several hundred meters to a kilometer in vertical (Atkins et al., 1995; Miller et al., 2003; Thompson et al., 2007). Furthermore, as both surface and meteorological conditions vary depending on the region and time of the year, sea breeze forecasting techniques developed for a specific region do not necessarily work well in another region (Miller & Keim, 2003).

As a persistent boundary layer feature existing along the inhomogeneous land-sea interface, the sea breeze responds to and interacts with various surface properties such as soil moisture (Baker et al., 2001), surface

roughness length (Kala et al., 2010), the coastline curvature (Boybeyi & Raman, 1992), and sea surface temperature (Lombardo et al., 2018; Seroka et al., 2018). Atmospheric parameters such as large-scale winds (Arritt, 1993), wind shear (Drobinski et al., 2011; Moncrieff & Liu, 1999), relative humidity (Rousseau-Rizzi et al., 2017), and low-level instability (Xian & Pielke, 1991) play important roles as well. The sea breeze can be influenced by preexisting boundary layer processes such as river breezes (Zhong et al., 1991), Rayleigh-Bénard convective thermals (Ogawa et al., 2003; Rochetin et al., 2017), horizontal convective rolls (Atkins et al., 1995; Fovell, 2005), and convective cold pool boundaries (Kingsmill, 1995; Rieck et al., 2015; Soderholm et al., 2016; Wilson & Megenhardt, 1997). Since these environmental properties and boundary layer processes covary and interact with one another in time and space, they introduce significant uncertainties both in the initial condition and prognostic fields of numerical simulations.

Although several numerical experiments have demonstrated the individual impacts of the surface and atmospheric layer properties on the sea breeze convection, only a few studies (e.g., Baker et al., 2001; Darby et al., 2002; Grant & van den Heever, 2014) have assessed both the individual influences of parameters and their interactions by perturbing two or more parameters (i.e., factor separation technique by Stein & Alpert, 1993), the uncertainty ranges of which tended to be coarse. A comprehensive assessment of the relative influences of the many environmental parameters impacting sea breezes and their synergistic interactions is scarce and hence forecasting the timing, location, and intensity of sea breeze convection remains a challenging problem that is worthy of more in-depth inquiry.

The extent and the intensity of the sea breeze have received considerable attention due to their role in the redistribution of near-surface aerosols (Blumenthal et al., 1978; Edinger & Helvey, 1961; Lu & Turco, 1994; Verma et al., 2016). Near-surface aerosols can be transported further inland and/or higher aloft through inland propagation and/or frontal uplift, respectively (Lyons et al., 1995; Thompson et al., 2007). While aerosol redistribution within the boundary layer has been studied extensively (Banta et al., 2011; Ding et al., 2004; Iwai et al., 2011; Liu et al., 2001; Loughner et al., 2014), the convective processes that may redistribute aerosols further aloft have received little attention. This is particularly true in observational studies using in situ measurements where sea breeze cases accompanying convective clouds and precipitation have been excluded from the analysis, since those signals generate substantial aerosol backscatter gradients which hinder the retrieval of boundary layer and aerosol properties (Caicedo et al., 2019). In the presence of moist sea breeze-initiated convection, aerosols in the lower troposphere may be vertically redistributed to upper tropospheric levels via cloud venting (Cotton et al., 1995). It is, therefore, necessary to identify the response of the sea breeze convection and associated aerosol redistribution via convective processes to different environmental parameters, including those that may be altered by anthropogenic activity in these already populated coastal regions.

Primarily due to the computationally intensive nature of the problem, few studies have considered the sensitivities of the sea breeze convection over a multidimensional parameter space where simultaneous parameter variations are allowed. Igel et al. (2018, hereafter IvJ18) explored this problem as part of the Holistic Analysis of Aerosols in Littoral Environments (HAALE) team effort, an Office of Naval Research (ONR)-funded Multidisciplinary University Research Initiative (MURI). One of the primary goals of the HAALE-MURI team has been to characterize the fundamental environmental parameters that control aerosol redistribution in littoral (coastal) zones in order to aid the development of coupled data assimilation systems. IvJ18 quantified the percentage contribution of 11 environmental parameters to sea breeze characteristics and aerosol redistribution in a dry, cloud-free subtropical environment. The present study extends the work of IvJ18 by examining a moist coastal rainforest environment that supports the development of both diurnal and sea breeze-initiated convective clouds and precipitation over land.

This research seeks to answer the following questions: in a moist coastal rainforest environment, what are the key environmental parameters that control the uncertainty in (1) the inland characteristics of sea breeze; (2) the intensity of the associated tropical sea breeze convection; and (3) the potential vertical redistribution of aerosols? We address these questions with an ensemble of idealized cloud-resolving model simulations and the application of the same statistical procedure used in IvJ18. Specifically, this procedure includes statistical emulation (O'Hagan, 2006), enabling prediction of the model output responses for a large number of untried parameter combinations, thereby allowing us to efficiently investigate a wide range of multidimensional parameter relationships. Finally, the controlling environmental parameters are characterized using

Table 1
A List of the Environmental Parameters Perturbed in This Study, Including the Ranges Selected

	Uncertainty range	
Parameter	This Study	IvJ18
Atmospheric	Moist tropical	Arid subtropical
Inversion layer strength	1–15 K km^{-1}	
Inversion layer depth	100–1,000 m	
Boundary layer potential temperature	285–300 K	
Boundary layer relative humidity	75–95%	20–50%
Boundary layer height	100–1,000 m	
Initial wind speed	−5–5 m s^{-1}	
Surface	Rainforest	Desert
Sea-air temperature difference ($SST-T_{atm}$)	−10–10 K	
Sea surface temperature gradient (SST Gradient)	−0.02–0.02 K km^{-1}	
Land-air temperature different ($T_{land}-T_{atm}$)	0–10 K	
Soil saturation fraction	(0.1, 0.9) with the saturation volumetric moisture content of 0.420 m^3 m^{-3}, sandy clay loam	(0.1, 0.9) with the saturation volumetric moisture content of 0.395 m^3 m^{-3}, sandy soil

Note. Adapted from IvJ18 but for a moist tropical rainforest environment. See Table 1 in IvJ18 for detailed descriptions.

variance-based sensitivity analysis (Saltelli et al., 2000), which decomposes the overall variance in a model output variable into contributions from the individual parameters, as well as their interactions.

2. Methods

2.1. Choice of Perturbed Environmental Parameters

IvJ18 compiled six atmospheric and five surface characteristics that have previously been identified in the literature as important to sea breeze circulations (see Table 1 in IvJ18) and perturbed them to conduct the sensitivity experiments. To facilitate comparisons with IvJ18, we adopt 10 of those 11 parameters as initial conditions for each of the sea breeze simulations conducted here (Table 1). Each parameter has an uncertainty range, and we perturb these parameters simultaneously over their ranges to produce a perturbed parameter ensemble over the 10-dimensional parameter space. We assign to each parameter the same uncertainty range utilized in IvJ18, with the exception of the boundary layer humidity, which differs between the arid and moist environments. The latitude, which determines the Coriolis parameter and solar zenith angle, is excluded here since our focus is on tropical sea breezes.

Six atmospheric parameters are examined, and five of them are selected based on their potential impact on the moisture and instability available to the moist convection. These parameters are the thermodynamic characteristics of the boundary layer (potential temperature, relative humidity, and height) and those of the inversion layer (strength and depth). For the development of moist convection, higher values are assigned to the minimum and maximum values of the boundary layer relative humidity compared to IvJ18. The initial wind speed, which can exert strong control over sea breeze characteristics in different environments, is also considered (Crosman & Horel, 2010).

The impacts of four surface parameters are analyzed due to their potential effects on sea breeze characteristics and convective properties via the partitioning of the surface sensible and latent heat fluxes. These parameters are the sea-air temperature difference, sea surface temperature gradient, land-air temperature difference, and soil saturation fraction. Over both ocean and land surfaces, the surface temperature is varied by perturbing the temperature difference between surface temperature and the initial air temperature (i.e., initial boundary layer potential temperature) at the lowest atmospheric level. The horizontal gradient of the sea surface temperature is specified to linearly vary from the coast to further offshore with the uncertainty range of −0.02 to 0.02 K km^{-1}, based on the analysis by Reynolds et al. (2007). Soil saturation fraction is perturbed for all 11 soil levels with the same value.

2.2. Model Configuration

The Regional Atmospheric Modeling System (RAMS) is a three-dimensional, nonhydrostatic, fully compressible cloud-resolving model that has been successfully used to investigate sea breeze in a number of prior studies (e.g., Darby et al., 2002; Freitas et al., 2006; Grant & van den Heever, 2014; IvJ18; Miao et al., 2003). A suite of three-dimensional idealized simulations of sea breezes, where the 10 environmental parameters are simultaneously perturbed, is carried out using RAMS version 6.2.08 (Cotton et al., 2003). Details of the RAMS parameter settings and grid configuration discussed below are all included in Table 2. The spatial resolution chosen here is fine enough to represent the detailed sea breeze structure (Crosman & Horel, 2010) while still being computationally feasible for a large ensemble approach. To ensure that a land breeze develops before dawn and a sea breeze develops during the day, thereby capturing one full diurnal cycle of the sea breeze, the model is integrated for 24 hr, beginning at 0000 local time (LT). The RAMS output responses from the regions within 250 km of the zonal borders are removed from the analysis to exclude any potential uncertainties associated with lateral boundary conditions.

Table 2
RAMS Model Setup

Model aspect	Setting
Grid	• 1,500 (zonal) × 150 (meridional) points • $\Delta x = \Delta y = 1$ km • 57 vertical levels; model top ~26 km • $\Delta z = 100$ m near the surface increasing to 1 km near the model top
Integration	• 3 s time step • 24 hr simulation duration beginning at 0000 local time (LT) • Sunrise at 0600 LT and sunset at 1800 LT
Surface parameterization	• Land-Ecosystem-Atmosphere-Feedback version 3 (LEAF-3, Walko et al., 2000) • Eastern half of the domain: flat ocean with fixed sea surface temperature (SST) and horizontal gradient of SST • Western half of the domain: flat land surface; evergreen broadleaf surface type (vegetation fraction = 0.90, vegetation height = 32 m, surface roughness length = 3.5 m) with sandy clay loam soil • Eleven soil levels from 0.01 to 0.5 m below ground • Straight coastline stretching north-south at the midpoint in the zonal direction ($x = 750$ km, black dashed line in Figure 3)
Initialization	• Thermodynamic profile: horizontally homogenous • Wind profile: horizontally homogenous, oriented perpendicular to the coastline without vertical shear • Random temperature perturbations within the lowest 500 m of the domain with a maximum perturbation of 0.1 K at the surface • Aerosol profile: horizontally homogeneous and exponentially decreasing with height with a maximum concentration of 500 mg^{-1} at the surface
Boundary conditions	• Open-radiative in zonal direction • Periodic in meridional direction
Radiation parametrization	• Two-stream (Harrington, 1997), updated every 60 s
Microphysics parameterization	• Double-moment bin-emulating bulk scheme with eight hydrometeors (Meyers et al., 1997; Saleeby & Cotton, 2004; Saleeby & van den Heever, 2013; Walko et al., 1995)
Aerosol treatment	• Ammonium sulfate • Radiatively and microphysically active • Sources and sinks
Coriolis	No ($f = 0$)

RAMS is coupled to the Land-Ecosystem-Atmosphere-Feedback Version 3 (LEAF-3, Walko et al., 2000), an interactive land-surface model that is comprised of different surface vegetation types and soil classes. LEAF-3 prognoses temperature and moisture fields for 11 soil levels and the vegetation canopy. Furthermore, through the two-way interactive coupling, the land surface and atmosphere can interact via the exchanges of momentum, heat, moisture, and radiative fluxes, as well as transpiration and precipitation. For example, precipitation over land can modulate the spatial distribution of soil moisture, thereby altering the partition of surface fluxes. Then the changes in these fluxes feed back to the atmosphere and hence can impact the development of convective clouds and precipitation.

We use the same surface configurations used in Grant and van den Heever (2014, hereafter GvdH14) to represent tropical rainforests such as those found in the coastal Cameroon region (Table 2). The surface configurations are significantly different from those used in IvJ18 (i.e., a bare desert surface type where vegetation is absent and with a surface roughness length of 0.07 m). As such, we can investigate sea breezes and convection over vegetated land surfaces in which friction and evapotranspiration can play an important role.

The initial horizontally homogeneous thermodynamic profiles for our simulations (Figure 1) are based on representative profiles derived for tropical coastal environments, allowing for the development of convective clouds and precipitation. Specifically, we adapt the initial thermodynamic profile used in GvdH14 (see Figure 1 of GvdH14), which is representative of equatorial Africa's summer months (June–August). Given the idealized nature of our framework, initial conditions are chosen to broadly represent moist coastal regimes, and not to represent a particular event over a tropical coastal rainforest. While utilizing the upper-tropospheric thermodynamic profile from GvdH14, we perturb the lower-tropospheric characteristics such as boundary layer potential temperature, relative humidity, and height, as well as the inversion layer strength and depth.

Within the boundary layer, whose vertical extent is determined by the initial boundary layer height, the relative humidity and potential temperature are held constant with height. The initial relative humidity is made

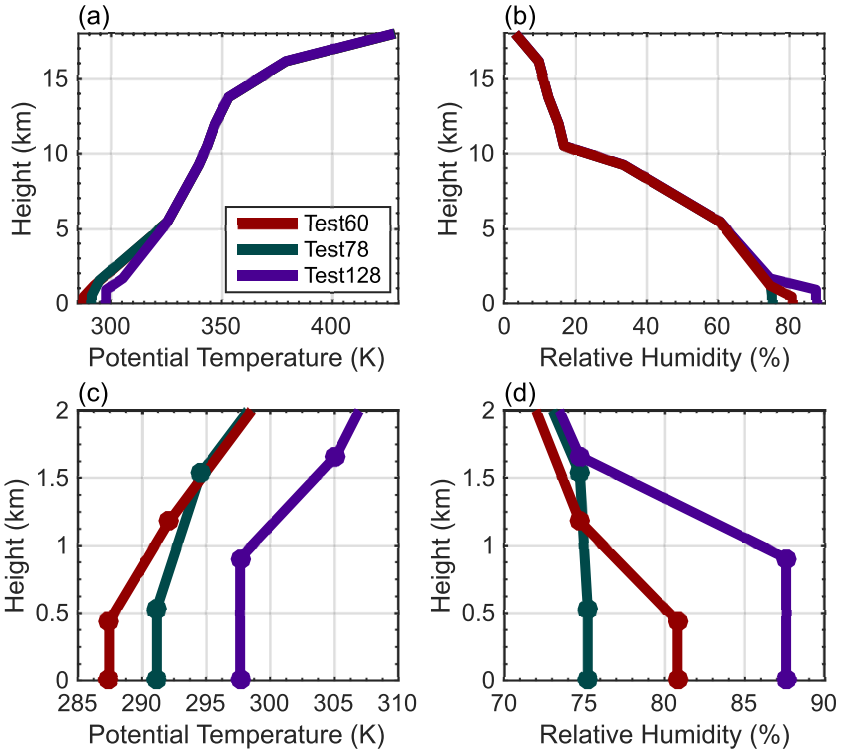

Figure 1. Example initial thermodynamic profiles from Tests 60 (red), 78 (green), and 128 (purple) of the 130 ensemble members: (a) Potential temperature profiles and (b) relative humidity profiles. The upper-tropospheric relative humidity and potential temperature profiles are kept identical above the inversion layer for all simulations, based on GvdH14. In the GvdH14 sounding, the relative humidity becomes less than 75% at 600 hPa, which is the minimum value over the parameter uncertainty range. At the same time, the potential temperature first exceeds 315 K, which is the maximum value for the inversion top, considering the uncertainty ranges of the parameters. Panels (c) and (d) show the lowest 2 km of panels (a) and (b), respectively. Filled circles in (c) and (d) indicate the base of the boundary layer, the base of the inversion layer, and the top of the inversion layer.

vertically homogeneous to ensure that we never initialize a simulation with supersaturated conditions. At the top of the boundary layer, the inversion layer begins immediately, and the potential temperature is increased linearly with height within the inversion layer. Example initial thermodynamic profiles from three of the 130 simulations are shown in Figure 1. Random temperature perturbations, which break the homogeneity of the initial thermodynamic conditions thereby permitting the realistic development of the idealized sea breezes, are introduced to the potential temperature field.

A passive tracer, serving as a proxy for the aerosol field, is introduced with concentrations identical to the initial ammonium sulfate distribution. This tracer field is not microphysically active but can be transported by the three-dimensional wind field. Therefore, the tracer field represents particles that do not serve as cloud condensation nuclei and which are not scavenged, but are vertically and horizontally transported. Hence, it allows us to take the first steps in visualizing and quantifying the dispersion and transport of aerosols while reducing the complexity introduced as a result of microphysical interactions.

2.3. Statistical Analysis Methodology

The proposed science questions are addressed through the application of a statistical procedure. This approach enables us to quantify the response of model output to individual input parameters and their interactions over the 10-dimensional parameter uncertainty space at a relatively low computational expense. This statistical framework has been successfully employed in several previous modeling studies (Lee et al., 2011, 2013; Johnson et al., 2015; IvJ18; Wellmann et al., 2018) that have assessed the relative importance of simultaneously perturbed input parameters to modeled responses. This statistical procedure is composed of three major steps (see Figure 1 of Lee et al., 2011): statistical experiment design, statistical emulation, and variance-based sensitivity analysis.

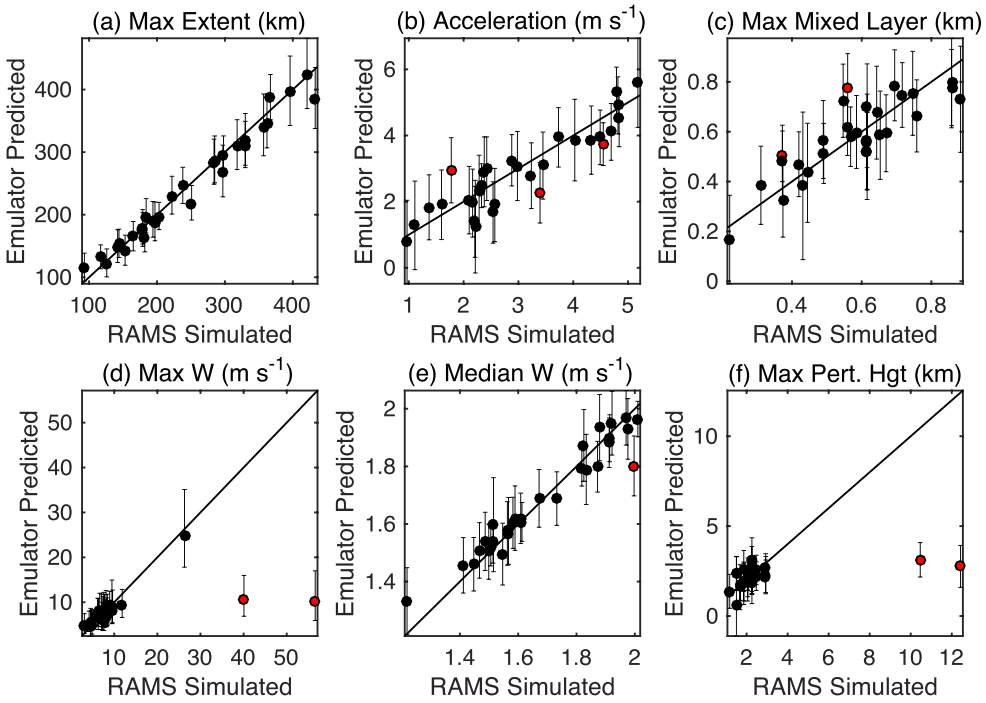

Figure 2. Emulator validation for six outputs of interest: (a) maximum inland extent, (b) sea breeze acceleration, (c) maximum mixed-layer depth, (d) maximum updraft speed, (e) median updraft speed, and (f) maximum tracer perturbation height. For each RAMS model output of interest, the values explicitly simulated from 30 reserved RAMS simulations out of the ensemble (*x* axis) are plotted against that predicted by the emulator (*y* axis). The error bars are 95% confidence bounds on the emulator predictions. The solid line is the 1:1 line of agreement. Outliers are marked in red.

The statistical procedure begins with the design of a perturbed parameter ensemble of simulations—a set of simulations in which the parameters are perturbed over their uncertainty ranges simultaneously to cover the multidimensional parameter uncertainty space. The selected input combinations of the parameters for each ensemble member correspond to the initial conditions of a RAMS sea breeze simulation. We utilize a space-filling algorithm called maximin Latin Hypercube sampling (Morris & Mitchell, 1995), which generates simultaneous variations of the input parameters while ensuring good coverage of the multidimensional parameter space with a minimum number of parameter combinations. We generate 130 combinations of the parameters in Table 1 and use them to initialize and run 130 sensitivity simulations of sea breeze convection with RAMS.

The next step in this approach is the construction of a statistical emulator (O'Hagan, 2006) for each of the output variables. Emulators are used to act as statistical surrogates of the RAMS simulator, where for each model output an emulator maps the relationship between the uncertain input parameters and the output response over the entire parameter uncertainty space. For each RAMS output variable of interest, we construct an emulator using the statistical software R (R Core Team, 2017) and the DiceKriging package (Roustant et al., 2012). The information from the first 100 RAMS simulations in our perturbed parameter ensemble (the "training set") is used to build an emulator. We then validate the statistical robustness of each emulator and its ability to produce a reasonable representation of the RAMS output response using the remaining 30 RAMS simulations (the "validation set"). As depicted in Figure 2, we compare RAMS output responses from the validation set with corresponding emulator predictions. The emulator is considered valid when at least 90% of the RAMS simulated "true" output values (values on the abscissa in Figure 2) lie within the 95% confidence bounds of the corresponding emulator prediction (values on the ordinate in Figure 2), and these values follow along the line of equality (solid black lines in Figure 2).

Emulators for the maximum inland extent of the sea breeze front (Figure 2a) and the median updraft speed (Figure 2e) satisfy the validation criteria very well. For the sea breeze acceleration (Figure 2b) and the maximum mixed layer depth (Figure 2c), the emulator predictions are noisier but still capture the overall signal

and following the line-of-equality reasonably well. When there is a sharp regime shift that leads to substantial variability in the output over an area of parameter space, the constructed emulator can struggle to capture the model response. For example, as shown in Figures 2d and 2f (the maximum updraft speed and maximum tracer perturbation height, respectively), the validation data set looks acceptable at all points except those highlighted in red. These outliers are associated with the sharp convective behavior changes that occur when the initial boundary layer potential temperature is at the upper end of its range (~298 K). In these cases we do not sample from the emulator where the emulator prediction is vastly underestimating the model output, and hence the contribution to output variance from the initial boundary layer potential temperature is likely underestimated for them.

Finally, variance-based sensitivity analysis (Saltelli et al., 2000) is performed to decompose the overall variance in a given RAMS output variable into contributions from individual parameters and their interactions. Utilizing the validated emulators, we sample the model output response across the 10-dimensional parameter space. We then compute the variance decomposition measures using the extended-Fourier Amplitude Sensitivity Test method (Saltelli et al., 1999) in the R package "sensitivity" (Pujol et al., 2013).

3. Results

3.1. Overview of the Sea Breeze Characteristics and Convective Morphology

As the extent and intensity of sea breeze convection are different among the 130 simulations, a summary of the sea breeze characteristics and the convective morphologies is given here.

3.1.1. Inland Propagation Characteristics

First, we consider the characteristics of the inland propagation of the sea breeze. In all of the 130 simulations in our ensemble, sea breeze convergence develops, and the inland propagation of each sea breeze front is objectively identified every 10 min using the identification algorithm developed by IvJ18. This algorithm uses the meridionally averaged surface fields of potential temperature and zonal wind speed to track the sea breeze convergence (see Appendix A in IvJ18 for further details).

An example of the identified inland location of the sea breeze front is shown in Figure 3a on the Hovmöller diagram of the meridionally averaged surface zonal wind speed. We define the time when the algorithm first identifies the sea breeze front as the onset of the sea breeze for all simulations. The last algorithm-identified location represents the maximum inland penetration distance of the sea breeze front, and consequently, the maximum distance that the near-surface pollutants can be horizontally advected over land through the dynamics of the sea breeze. The ensemble-mean of the maximum inland extent is 243.8 km with a standard deviation of 84.6 km, which indicates that there is a considerable amount of variation in the sea breeze evolution across the ensemble. The range of the maximum inland extent in the simulations is within the range of previously observed moist tropical sea breeze extents, as discussed above (Clarke, 1983; Muppa et al., 2012; Physick & Smith, 1985).

It is known that sea breezes propagate slower during the daytime than at night since the turbulence ahead of the front associated with the daytime surface heating and convection acts as a drag, slowing the inland propagation of the sea breeze (Physick & Smith, 1985; Reible et al., 1993; Simpson et al., 1977). The speed of the inland penetration thus decreases in the afternoon due to the enhanced turbulent mixing and increases after sunset due to the decreased turbulence (Tijm et al., 1999). As in IvJ18, we define the daytime propagation speed by dividing the inland location of the sea breeze front at sunset by the total time that the sea breeze has existed from onset to sunset ($\frac{\text{inland extent at 1800 LT}}{\text{1800 LT} - \text{onset}}$). The nighttime propagation speed is computed as the final location of the sea breeze front divided by the time interval from sunset to the final time that sea breeze is identifiable. In all simulations, the daytime propagation speed is less than the nighttime propagation speed. The ensemble-mean $\pm$ standard deviation daytime and nighttime propagation speeds are computed as 3.3 ± 1.3 and 6.2 ± 2.0 m s^{-1}, respectively. We took the difference between the nighttime and the daytime propagation speed of the sea breeze front as a proxy of the sea breeze acceleration and examine this metric to demonstrate the impact of daytime turbulence on the sea breeze propagation.

The inland advection of a relatively cold and stable marine air mass suppresses the development of the convective mixed layer over land within the air mass, as shown in Figure 3b, demonstrating lower surface-based mixed layer depths behind the sea breeze front compared to that ahead of the front. The maximum depth of

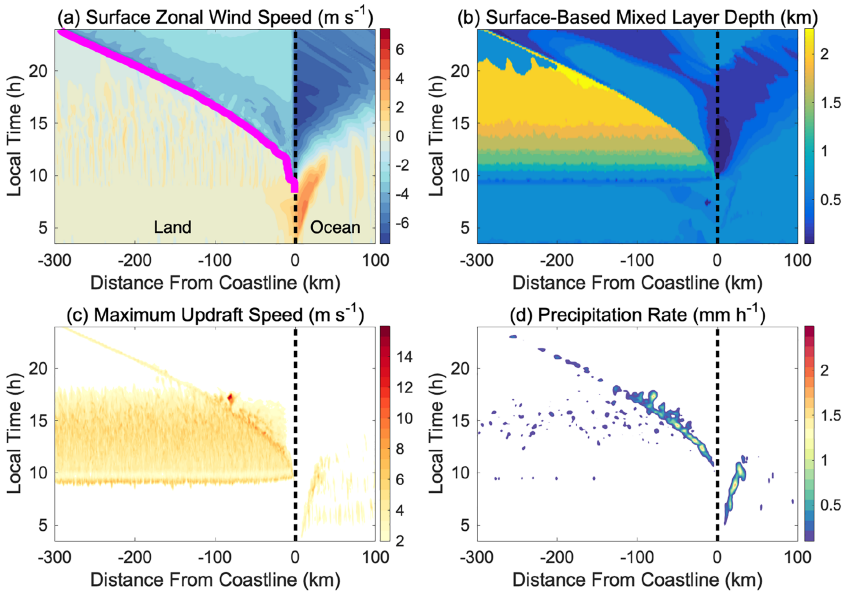

Figure 3. Hovmöller diagrams of (a) meridionally averaged surface zonal wind speed (m s^{-1}), (b) surface-based mixed layer depth (km), (c) maximum updraft speed (m s^{-1}), and (d) meridionally averaged precipitation rate (mm hr^{-1}) from Test 37. These figures demonstrate an example of the tracked evolution of the sea breeze front in this case. The land is on the left side of the domain and the ocean is on the right side, and as such the sea breeze front advances to the left (westward) as time advances upward on the ordinate. The magenta line denotes the horizontal location of a sea breeze front objectively identified every 10 simulation minutes. The black dashed line at $x = 0$ km denotes the forest-ocean border. Only a portion of the grid domain is shown.

this suppressed mixed layer behind the sea breeze front is also analyzed to describe the stability of the air mass adjacent to the sea breeze front, which can potentially impact the frontogenesis/frontolysis. Surface-based mixed layer depth is identified using the meridionally averaged potential temperature field at each model output time and is defined as the height above the surface at which the vertical potential temperature gradient first exceeds 2 K km^{-1} (IvJ18). The diurnal variations in the mixed-layer depth are well captured with a 2 K km^{-1} threshold, and while other threshold values were tested, they did not qualitatively change the results.

3.1.2. Convective Characteristics

We now examine the characteristics of the convection developing over land during the daytime (from onset to sunset) along and ahead of the sea breeze. At the sea breeze front, the sea breeze convergence induces vertical lifting, one of the key ingredients for moist convection (Doswell, 2001). An example of a Hovmöller diagram of maximum updraft speeds from one of the ensemble members clearly shows the most vigorous updrafts along the front (Figure 3c). For the same simulation, a Hovmöller diagram of the meridionally averaged precipitation rate is presented in Figure 3d, illustrating that the heaviest rainfall is also localized along the sea breeze front, while lighter rainfall associated with the daytime boundary layer convection occurs ahead of the sea breeze front.

Figure 4a displays the frequency distributions of the low (<4 km), middle (4–7 km), and high (>7 km) clouds for each simulation based on the cloud top height. We define the cloud top height in each column as the highest height at which the total condensate exceeds 0.1 g kg^{-1}. Lower thresholds are not used to avoid capturing the top of cirrus clouds. The neighboring columns are checked as well for the presence of condensate. In the majority of simulations, the percentage occurrence of the low clouds (gray bars) significantly exceeds that of the middle (cyan bars) or high clouds (magenta bars), which indicates the dominance of the low cloud regime. No middle and high clouds develop in 104 out of 130 simulations, and thus the maximum cloud top height of these simulations is lower than 4 km (Figure 4b). In 12 of the 130 simulations, the frequency occurrence of high clouds is greater than zero, and these simulations are also marked with maximum cloud top heights greater than 7 km (Figure 4b).

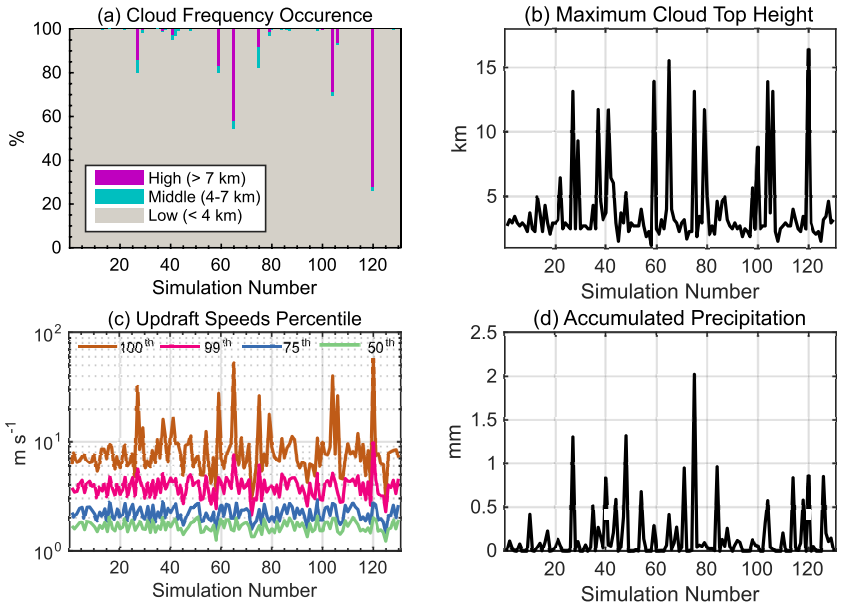

Figure 4. Summary of convective morphologies during the daytime over the land region: (a) cumulative frequency of occurrence (%) of low (<4 km, gray bars), middle (4–7 km, cyan bars), and high (>7 km, magenta bars) clouds where the sum of these three make 100%; (b) maximum cloud top height (km); (c) percentiles of updraft velocity for all grid points where the vertical velocity is greater than or equal to 1.0 m s^{-1} (log-scaled); and (d) land-averaged accumulated surface precipitation at sunset.

Figure 4c shows the different percentiles of updraft speeds greater than or equal to 1 m s^{-1}. The sensitivity of different percentiles to different updraft speed thresholds was evaluated and did not qualitatively change the results. The peaks in the maximum updraft speed correspond with those peaks evident in the simulations with high clouds. For the 50th–99th percentiles, the updraft speeds do not exceed 10 m s^{-1} in any of the simulations (Figure 4c). While the updraft speeds and cloud top heights show a close correspondence, the land-averaged accumulated precipitation does not always match those peaks in cloud top height or updraft maxima (Figure 4d). Furthermore, the land-averaged accumulate precipitation is lower than 0.1 mm in 94 out of 130 simulations. As such, there is no distinct relationship between individual input parameters and land-averaged accumulate precipitation revealed from pairwise scatter plots (not shown), and the emulator approach is not applicable.

A graphical example of the convective morphologies that develop is illustrated in the three-dimensional condensate fields in Figure 5. Two examples are chosen here to illustrate two cases where the sea breeze-initiated convection is shallow (Figure 5a) and deep (Figure 5b), respectively. In both cases, the deepest clouds and heaviest precipitation are collocated and localized along the sea breeze convergence. However, in the shallow case (Figure 5a), shallow clouds are prevalent over land, both ahead of and along the sea breeze front, and only the latter clouds produce precipitation. In the deep case (Figure 5b), the sea breeze-initiated deep convective development and anvils are evident. Moreover, boundary layer convection marked by shallow clouds ahead of the sea breeze front also produce precipitation in this deep case.

Altogether, in our ensemble, daytime boundary layer convection producing relatively lower clouds, weaker updrafts, and weaker precipitation are prevalent over land, particularly ahead of the sea breeze. In contrast, the stronger convection accompanying the highest cloud tops, strongest updrafts, and heavier precipitation is focused along the sea breeze convergence. Even though the boundary layer convection is not directly linked to the sea breeze convergence, they have a potential impact on the preconditioning of the sea breeze-initiated convection, via boundary layer mixing (Fankhauser et al., 1995), cumulus formation (Waite & Khouider, 2010), and cold pool development (Wilson & Megenhardt, 1997).

3.2. Sensitivity Analysis: Inland Propagation Characteristics of the Sea Breeze

In this section, the sensitivity of the inland extent of the sea breeze is demonstrated. In particular, to facilitate direct comparison with the IvJ18 study, the same three model outputs are examined: (1) the maximum

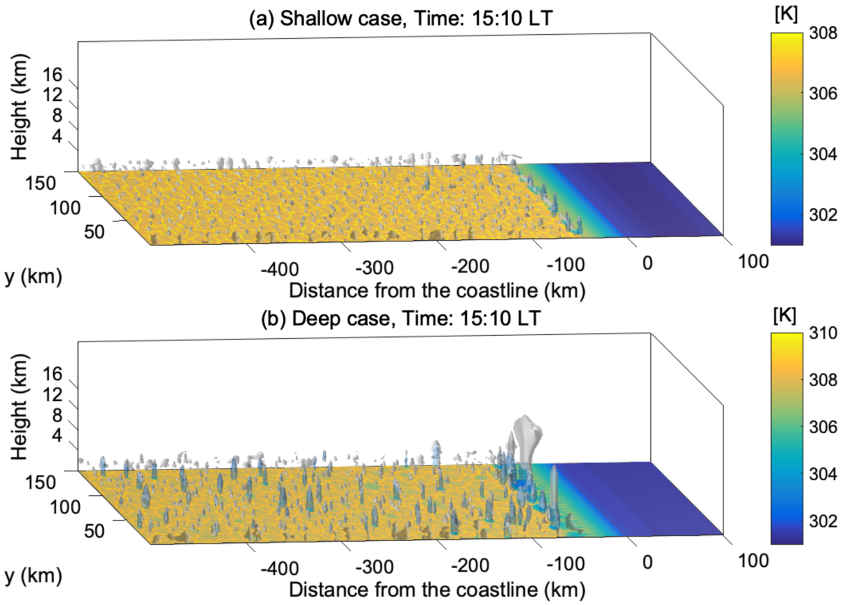

Figure 5. Example convective morphologies from a simulation where sea breeze-initiated convection is (a) shallow (Test 80) and (b) deep (Test 59) at 15:10 LT. White isosurfaces are where total condensate except for rain is 0.1 g kg^{-1}, and blue isosurfaces are where rain mixing ratio is 0.1 g kg^{-1}. Shaded contours are the density potential temperature (K, Emanuel, 1994) at the surface.

inland extent of the sea breeze, (2) the sea breeze acceleration, and (3) the maximum mixed layer depth behind the sea breeze.

Throughout the following sections, the variance-based sensitivity analysis results are presented as stacked, color-coded bar graphs to demonstrate the relative contributions of the 10 environmental parameters to the variance in the output parameter being examined (see the legend in Figure 6). In order to understand how the dominant parameters drive the changes in the output response, the mean response of each output to the environmental parameters that contribute 5% or more to the output variance is demonstrated.

Over the 10-dimensional parameter uncertainty range here, for each fixed value of a given parameter, we make 500 emulator predictions. A set of 500 response surfaces records the predicted output at each of these combinations for each response surface. An average of this large set of output data is then taken to determine the mean response.

3.2.1. Maximum Inland Extent

Initial wind speed dominates the variance in the maximum inland extent of the sea breeze front, explaining 85% thereof (Figure 6a). The mean response of the maximum inland extent to the initial wind speed (Figure 7a) shows that the sea breeze front propagates further inland when the initial wind is onshore (negative values), and vice versa. This response agrees with many previous studies, thus demonstrating the intuitive notion that strong offshore ambient flow inhibits the inland propagation of the sea breeze front (Arritt, 1993; Finkele, 1998; Porson et al., 2007; IvJ18). At the same time, when the ambient flow is offshore, it enhances convergence at the sea breeze front supporting frontogenesis (Reible et al., 1993).

Soil saturation fraction is the second-most-important parameter contributing to the variance in the maximum inland penetration of the sea breeze front (7%, Figure 6a). The sea breeze front propagates further inland in drier soil conditions (Figure 7b). When the soil is drier, the sensible heat fluxes over the land surface are enhanced while the latent heat fluxes are reduced due to less evapotranspiration. As a result, the land surface temperature increases in drier conditions, and hence, the horizontal temperature gradient between the land and ocean regions, which is the primary driver of the sea breeze formation and propagation, increases as well. The variance-based sensitivity analysis for the maximum horizontal temperature gradient (not shown) also identifies the soil saturation fraction as being the most influential parameter in determining the maximum thermal gradient.

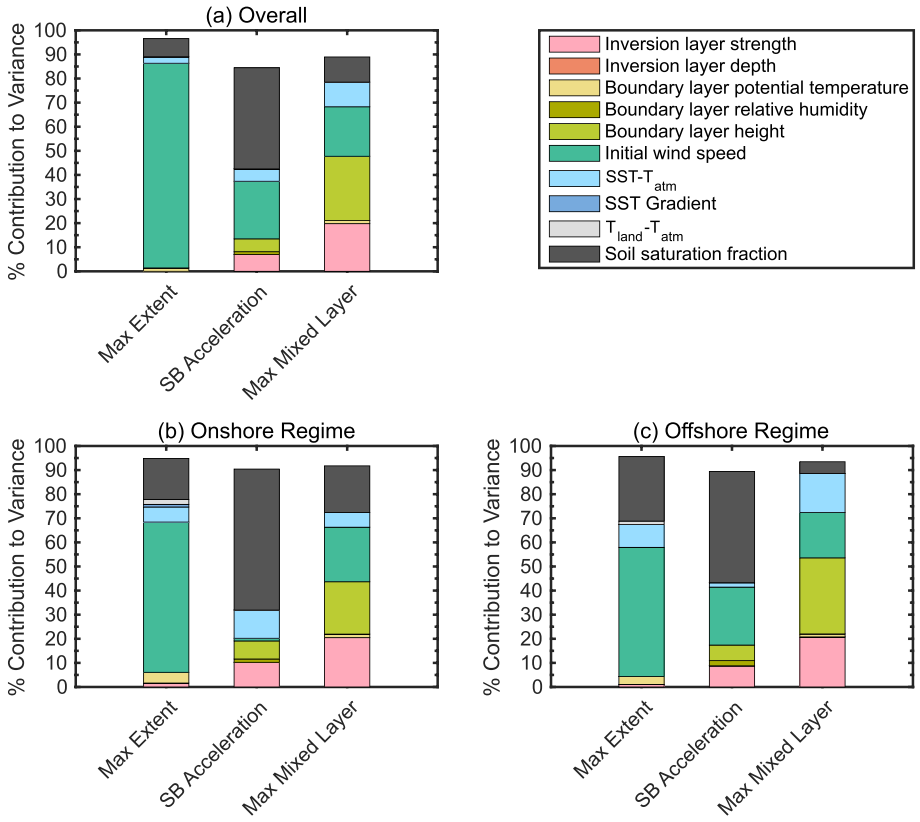

Figure 6. Percentage contribution to the variance of maximum sea breeze inland extent (left stacked bar), nighttime minus daytime propagation speed (middle stacked bar), and the maximum surface-based mixed layer depth behind the sea breeze front (right stacked bar) caused by each of the 10 parameters of interest over (a) the entire uncertainty parameter space, (b) the onshore regime only (initial wind speeds $\leq$0 m s^{-1}), and (c) the offshore regime only (initial wind speeds $\geq$0 m s^{-1}). Only those parameters which contribute to at least 1% of the variance are indicated. The height of each stacked bar indicates the summation of individual contributions to the output uncertainty from the 10 parameters. If the height is less than 100% this means that there are further contributions to the parameter variance arising from interactions among the parameters.

In IvJ18, the initial wind speed is also found to be the key parameter in determining the maximum sea breeze inland extent, accounting for 75% of the variance. Soil saturation fraction and sea-air temperature difference are also found to be important, contributing 13% and 7% to the output variance, respectively. While initial

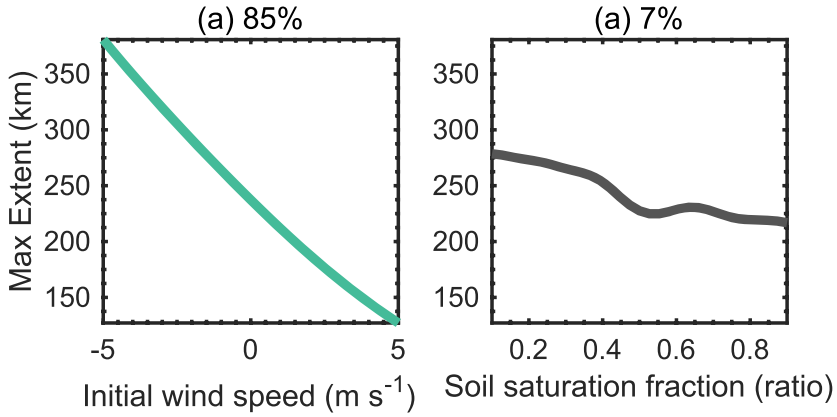

Figure 7. Mean responses of the maximum sea breeze inland extent to the parameters that contribute 5% or more to the output variance: (a) initial wind speed and (b) soil saturation fraction. Numbers at the top of each plot indicate the percentage contribution of each parameter to the output variance.

wind speed and soil saturation fraction are identified as being critical in our analysis as well, the influence of the sea-air temperature difference on the maximum inland extent is not found to be significant here. Overall, the relative importance of surface parameters (i.e., soil saturation and sea-air temperature difference) on the inland extent is greater in IvJ18 than in this study.

We hypothesize here as to why surface parameters are relatively more important for the maximum inland extent in a dry environment than in the moist environment. In the moist environment, shallow boundary layer clouds form over both land and ocean via boundary layer mixing, thereby reducing the incoming shortwave radiation absorbed at the surface. Additionally, surface vegetation, which is absent in IvJ18, responds to the incoming shortwave radiation via evapotranspiration. In other words, the land surface is more effectively heated in an arid desert environment, thereby directly determining the ocean-land thermal contrast. Therefore, the surface properties more directly influence the development and propagation of the incipient sea breeze front in the dry environment compared to the moist environment, where a number of other parameters modulate the role of the surface parameters.

3.2.2. Sea Breeze Acceleration

For the sea breeze acceleration, the key parameters vary between the analysis over the full parameter uncertainty space (Figure 6a) and the analysis over two different wind regimes (Figures 6b and 6c). These wind regimes are defined based on the uncertainty range of the initial wind speed: -5 to 0 m s^{-1} corresponds to the onshore regime, and 0 to 5 m s^{-1} corresponds to the offshore regime. While key parameters for the maximum inland extent and the maximum mixed layer depth (see section 3.2.3) do not change as a function of the two wind regimes, the contribution of the initial wind speed to the sea breeze acceleration is almost absent in the onshore regime, with the contributions from inversion layer strength and sea-air temperature difference being more important (second stacked bar graph in Figure 6b).

In both the onshore and offshore regimes, soil saturation fraction is found to be the most important contributor to the sea breeze acceleration uncertainty, accounting for 35% and 48% of the variance, respectively. As shown in Figures 8a and 8e, the sea breeze acceleration increases when the soil saturation fraction is lower. Under drier soil conditions, the inland sea breeze propagation is reduced during the day due to enhanced boundary layer turbulence mixing processes, which are weaker in the wetter soil conditions. After sunset, drier soil cools down faster than wetter soil, and hence the turbulence over land surface disappears quicker in drier soil. With less drag ahead of it, sea breeze front propagates faster in the nighttime. Therefore, the difference between the nighttime and daytime is greater in drier soil. To support this explanation, we examine the surface sensible heat fluxes over dry and wet soil simulations (Figure 9). Figure 9 shows that dry soil simulations have higher surface sensible heat fluxes (i.e., more near-surface turbulence) during the daytime than the wet simulations. Also, the surface sensible heat flux increases faster in the morning and decreases faster in the late afternoon over dry soil than wet soil, as shown by the steep slope in Figure 9, supporting the explanation.

Two more parameters contribute at least 5% to the variance in the sea breeze acceleration, in both the onshore and offshore regimes: inversion layer strength (27% in onshore and 11% in offshore) and boundary layer height (7% in onshore and 9% on offshore). Sea breeze acceleration increases when the inversion is stronger (Figures 8b and 8g), and the boundary layer is shallower (Figures 8d and 8h). These initial conditions are associated with shallower mixed layers over land during the daytime (see section 3.2.3 for behind the sea breeze front), which indicate increases in the static stability of the air adjacent to the sea breeze front. The enhanced static stability inhibits the entrainment of the ambient environmental air into the sea breeze front. This entrainment can perturb the sharp gradient between the land and ocean air masses and reduce the thermal gradient across the sea breeze front during the daytime. Finally, the enhanced thermal gradient will result in the sea breeze propagating faster, especially at nighttime, when there is less drag from surface heat fluxes and convection.

In the onshore regime, the sea-air temperature difference is also a significant parameter, contributing 9% to the variance of the acceleration. In other words, the impact of the marine air mass that is advected inland along the sea breeze front is relatively more important in the onshore regime than the offshore regime. Figure 8c demonstrates that sea breeze acceleration increases when the sea surface temperature is colder than the initial air temperature at the lowest model level, and vice versa. Relatively warm ocean temperatures support deeper mixing (Figure 10e) and vice versa. Therefore, the mean response (Figure 8c) can be

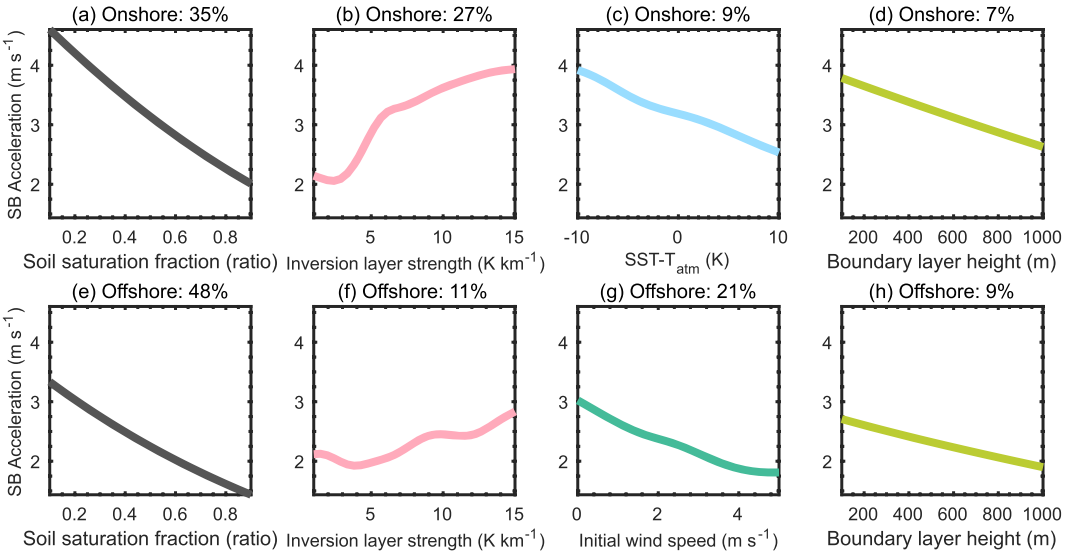

Figure 8. Mean responses of the sea breeze acceleration to the parameters that contribute 5% or more to the output variance in the onshore (a–d) and offshore (e–h) regimes. Numbers on the top of each plot indicate the percentage contribution of each parameter to the output variance.

related to the mean responses of the inversion layer strength and boundary layer height: suppressed development of the mixed layer behind the sea breeze front (see section 3.2.3) produces a greater thermal gradient between the land and ocean which results in the faster propagation of the sea breeze in the evening.

In the offshore regime, the sea breeze acceleration decreases when the offshore wind is stronger (Figure 8f). This response can be related to the "stagnation" of the sea breeze (Banta et al., 1993; Estoque, 1962). It appears that due to the stagnation effect in the stronger offshore wind flow, the difference between the nighttime and the daytime propagation speed is less notable compared to weaker offshore flow. The lower values in the mean responses of the sea breeze acceleration predicted over the offshore regime compared to the onshore regime also support this explanation.

In IvJ18, the initial wind speed, soil saturation, sea-air temperature difference, and Coriolis parameters were all found to be important for the sea breeze acceleration. The additional parameters of inversion layer strength and boundary layer height revealed in the moist regime can be explained as follows. A weaker inversion and a higher boundary layer result in stronger turbulent mixing, making the sea breeze more susceptible to entrainment and turbulence within the boundary layer.

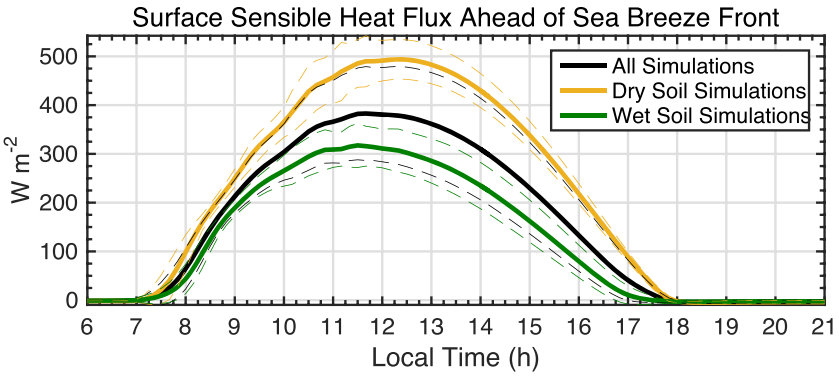

Figure 9. Time series of the land-averaged surface sensible heat flux (W m^{-2}) ahead of sea breeze front averaged from all simulations (black). Based on the permanent wilting point (i.e., the amount of soil moisture below which most plants will wilt and not be able to recover), simulations are separated into two groups: dry (soil saturation ratio ≤ 0.4, yellow lines) and wet (soil saturation ratio > 0.4, green lines). Dashed lines denote one standard deviation from the averaged sensible heat flux.

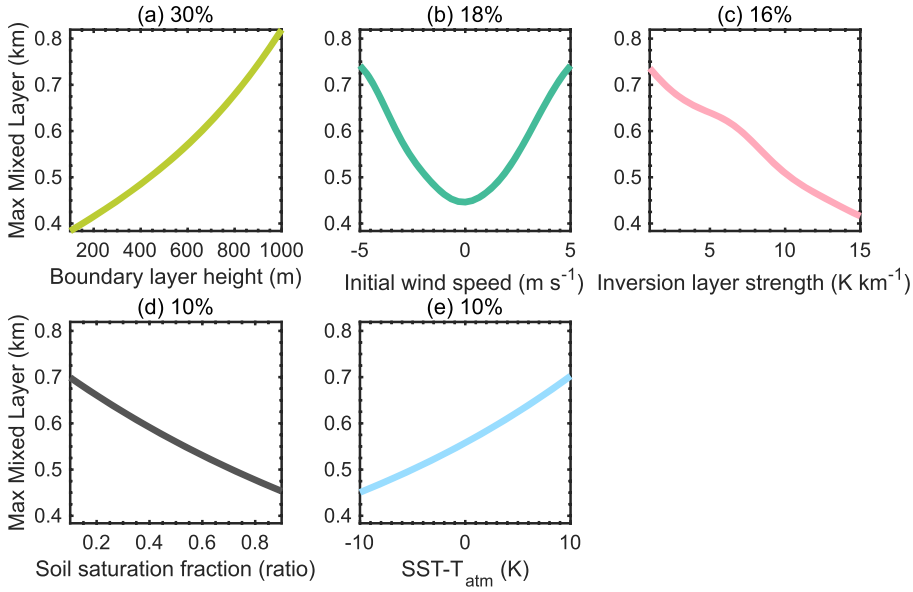

Figure 10. Mean responses of the maximum mixed layer depth behind the sea breeze front to the parameters that contribute 5% or more to the output variance: (a) boundary layer height, (b) initial wind speed, (c) inversion layer strength, (d) soil saturation fraction, and (e) sea-air temperature difference. Numbers on the top of each plot indicate the percentage contribution of each parameter to the output variance.

3.2.3. Maximum Mixed Layer Depth

The stacked bar graph on the right hand side in Figure 6a shows that there are five parameters contributing to more than 5% of the variance in the maximum mixed layer depth behind the sea breeze front: boundary layer height (30%), initial wind speed (18%), inversion layer strength (16%), soil saturation fraction (10%), and the sea-air temperature difference (10%). These contributions are similar in magnitude when the analysis is split into the onshore and offshore regimes (Figures 6b and 6c). Figure 10 shows that the maximum mixed layer depth behind the sea breeze front increases when the initial boundary layer is deeper, the initial wind is stronger regardless of the direction, the inversion is weaker, the soil is drier, and the sea surface is warmer than the air above it. The mean responses of the first four parameters are straightforward as they all promote deeper mixing of the boundary layer. For the sea-air temperature difference (Figure 10e), the warmer sea surface temperatures relative to the air above it promotes the mixing of air over the ocean, and that this deeper marine boundary layer air mass is advected inland through the inland propagation of the sea breeze.

IvJ18 revealed that the initial boundary layer height, inversion layer strength, and sea-air temperature difference are the controlling parameters for the maximum mixed layer depth in an arid sea breeze regime. The mean responses of the mixed layer depth to these parameters shown by IvJ18 are in agreement with the responses shown here for a moist regime. The initial wind speed and soil saturation fraction, which can influence surface sensible heat flux and boundary layer turbulence, are also found to be dominant in our analysis, in contrast to IvJ18. It would seem that the difference between these two studies can be attributed to the presence of the vegetation canopy, which is completely absent in IvJ18. The presence of the vegetation canopy increases the mechanical production of turbulence (Melas & Kambezidis, 1992) in addition to the convective turbulence, thereby assisting in deepening the boundary layer.

3.3. Sensitivity Analysis: Convective Intensity

In this section, we detail the impacts of our set of parameters on the intensity of the convection ahead of and along the sea breeze convergence, as quantified by updraft speeds. Here we look at the responses of the maximum and the median updraft speeds to represent the sensitivity of the sea breeze-initiated convection and daytime boundary layer convection, respectively.

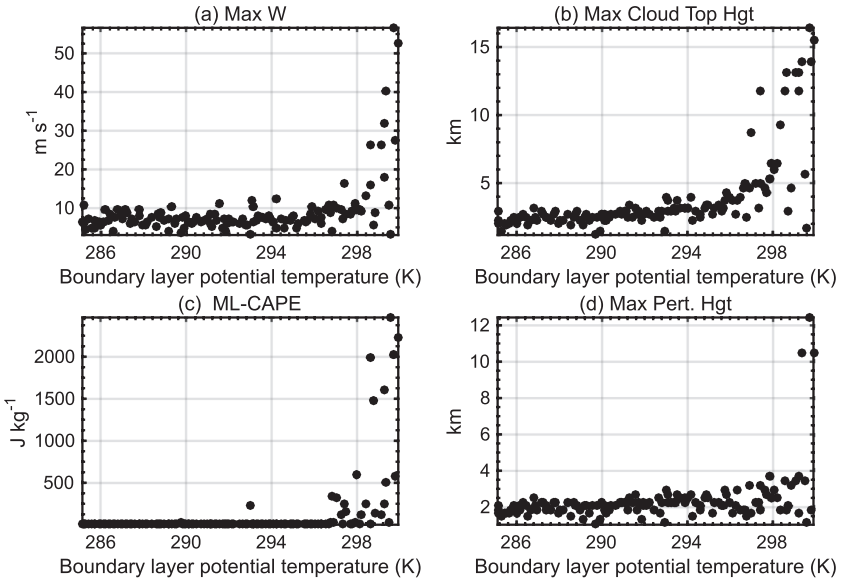

Figure 11. Pairwise scatterplots of the RAMS simulations for the (a) maximum updraft speed (m s^{-1}), (b) maximum cloud top height (km), (c) mixed-layer CAPE (J kg^{-1}), and (d) maximum tracer perturbation height versus the initial boundary layer potential temperature (K), showing two different convective regimes: shallow convection (<298 K) and deep convection (298–300 K).

3.3.1. Maximum Updraft Speed

Before performing the variance-based sensitivity analysis, we first explore pairwise scatterplots of the training and validation sets for all input-output combinations to see whether there is a regime shift separating shallow and deep convection. It is evident from Figures 11a and 11b that there are two convective regimes: shallow and deep regimes. The variability in the maximum updraft and the maximum cloud top height is small below 298 K, whereas there is a sharp transition from the weaker updrafts and shallow clouds to the strong updrafts and deep clouds around 298 K.

In the deep regime, the maximum updraft speed and the maximum cloud top height dramatically increase with the warmer boundary layer (Figures 11a and 11b). This result is not surprising given that the convective available potential energy (CAPE) is higher for the warmer boundary layer conditions in our environmental setup, all else being equal. Here we computed the mixed-layer CAPE at every output time step using spatially averaged soundings (from 10 km ahead of the sea breeze front to the western domain edge), and then temporally averaged these soundings from the sea breeze onset to sunset. Since by design the initial potential temperature profile above 5 km is identical in all of the simulations (Figure 1a), those simulations initialized with warmer boundary layer potential temperature have higher CAPE and are more likely to have deep convection. The pairwise scatterplot of the mixed-layer CAPE versus initial boundary layer potential temperature (Figure 11c) also illustrates that the CAPE behavior changes sharply for the warmer boundary layer within the strong updraft regime.

We now examine the sensitivity of the maximum updraft speed over the shallow convection regime to our 10 parameters. As stated in section 2.3, we perform the variance-based sensitivity analysis for the maximum updraft speed only over the shallow regime where the emulator predictions of the model output behavior are statistically robust (i.e., 285–297 K). In Figure 12, the height of the stacked bar graph is 75%, which indicates that parameter interactions contribute 25% to the output variance in the maximum updraft speed over the shallow regime.

Over the shallow regime, the initial inversion layer strength is the most influential uncertainty source of the maximum updraft speed, explaining 41% of the output variance (first stacked bar graph in Figure 12). The emulated mean responses of the maximum updraft speeds increase when the initial inversion is weaker (Figure 13a), and this response is perhaps not surprising given the role of capping inversions in limiting convective activity. The pairwise scatterplot of the maximum updraft speed over the shallow regime versus the

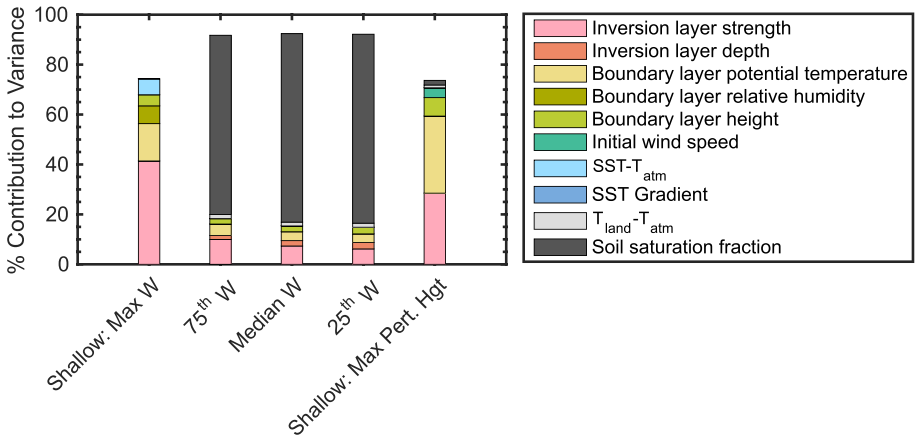

Figure 12. Percentage contribution to the variance by each of 10 parameters for the 100th (maximum), 75th, 50th (median), and 25th percentiles of updrafts speeds equal to or greater than 1.0 m s^{-1}, and the maximum tracer perturbation height. For maximum updraft speed and the maximum tracer perturbation height, the range of the initial boundary layer potential temperature was limited 285–297 K where the emulator approach was suitable. Only those parameters which cause at least 1% of the variance are indicated.

initial inversion layer strength clearly confirms that the emulator approach captures the updraft behavior over this regime (not shown).

The second-most-important parameter for the shallow regime maximum updraft speed is the initial boundary layer potential temperature, which accounts for 15% of the variance (first stacked bar graph in Figure 12). The warmer boundary layer favors stronger updrafts (Figure 13b). The warmer boundary layer enhances near-surface buoyancy and warms the near-surface air, thereby steepening the lapse rates of the lower troposphere. This enhanced low-level convective instability then can support the development of the boundary layer convection. The findings on the shallow regime are similar to those of Rousseau-Rizzi et al. (2017), who found that in a strongly inhibited environment, none of the initial parameters or the environmental conditions they considered are sufficient enough for the deep convection initiation along the mesoscale convergence line.

3.3.2. Median Updraft Speed

The height of the stacked bar graphs increase after the first one in Figure 12 and do not vary much, particularly from the 75th to 25th percentiles, thus indicating that parameter interactions do not play as large of a role in these updraft percentiles as in the case of the maximum updraft speeds. Moreover, the relative contributions of the parameters do not change between the median and the 25th percentiles. Therefore, we now only examine the responses of the median updraft speed to understand the sensitivity of the boundary layer convection.

For the median updraft speed, representative of the daytime boundary layer convection as discussed above, the key parameter is the soil saturation fraction, which explains 75% of the output variance, followed by the inversion layer strength which contributes 7% (third stacked bar graph in Figure 12). These two parameters are the most important in determining the average depth of the mixed layer ahead of the sea breeze (not shown), and hence the activity of the shallow convective mode (see Figure 5). The median updraft speed increases with lower soil saturation fraction and a weaker inversion (Figures 13c and 13d). Drier soil and weaker inversions promote turbulent mixing over the land during the daytime, thereby leading to stronger vertical motions in this convective mode.

3.4. Tracer Redistribution

We now investigate the impact of the 10 environmental parameters on the convective transport of aerosol over the land. We utilize passive tracers to represent our aerosol transport and define the tracer perturbation field as the difference in the number concentration of tracers between sunset and sunrise.

Similar to Figures 5a and 5b, Figures 14a and 14b show examples of the percentage perturbation field for simulations where sea breeze-initiated convection is shallow and deep, respectively. Positive (negative)

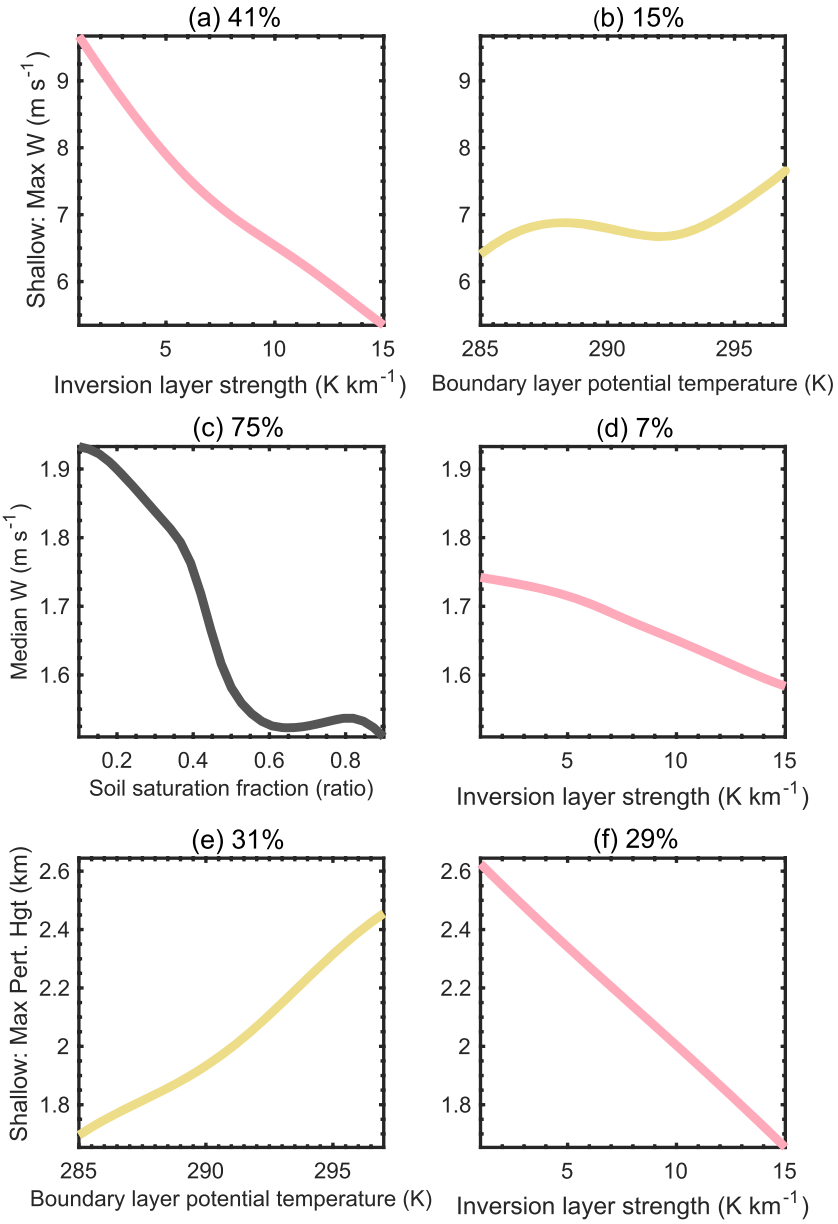

Figure 13. Mean responses of (a, b) the maximum updraft speed over the shallow convection regime, (c, d) median updraft speed, and (e, f) maximum tracer perturbation height to the top two parameters. Numbers at the top of each plot indicate the percentage contribution of each parameter to the output variance.

perturbations shaded with red (blue) indicate that tracer concentrations have been increased (decreased) relative to the sunrise concentration during the daytime. In both cases, negative perturbations exist near the surface with positive perturbations aloft.

The negative perturbations in both cases are stronger ahead of the sea breeze front at sunset (the location of which is shown using a pink star), where the diurnal boundary layer convection develops. During the daytime, boundary layer mixing over the land transports near-surface tracers to the boundary layer top, thereby producing the negative perturbation in the lower atmosphere and the positive perturbation aloft.

In the shallow case (Figure 14a), the positive perturbation above the boundary layer is impacted by the sea breeze front which assists in venting the aerosols out of the boundary layer, starting offshore. A similar structure has been documented in previous studies (e.g., IvJ18; Lu & Turco, 1994; Verma et al., 2006). In the deep

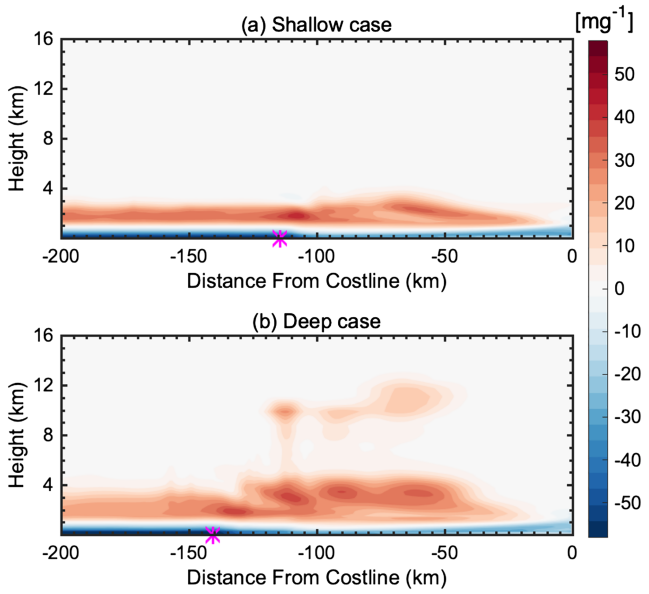

Figure 14. Examples of the tracer perturbation field (difference of the tracer concentration between sunset and sunrise) in a simulation where the sea breeze-initiated convection is (a) shallow (Test 80) and (b) deep (Test 59). The same simulations shown in Figure 5 are represented here. Pink asterisks along the *x* axis indicate the identified surface location of the sea breeze front at sunset in each case.

case (Figure 14b), the tracers are transported further upward in the presence of the more vigorous updrafts and deeper cloud extent. As for the maximum updraft speed, the emulator predictions are poor where deep convection develops in the presence of the sharp regime shift (Figures 2d and 11a). Therefore, we conduct the variance-based sensitivity analysis for the maximum tracer perturbation height over the shallow convection regime only (i.e., uncertainty range of the initial boundary layer is 285–297 K), where the emulator performs well.

Behind the sea breeze at sunset, weaker negative perturbations relative to those ahead of the sea breeze are observed. IvJ18 separated these two negative tracer perturbation plumes into one associated with boundary layer mixing and the other from horizontal sea breeze advection. However, in our ensembles, due to the complicated moist convective processes occurring over land, such plume separation is not feasible.

3.4.1. Convective Transport Intensity

We now look at the maximum positive perturbation height as an indicator of the intensity of the convective aerosol redistribution in the sea breeze regime. We determine this height by finding the height where the positive perturbation reaches its maximum value. The surface concentration behind the sea breeze at sunset, which is examined by IvJ18, is excluded here since it is difficult to obtain a statistically robust emulator.

Over the deep regime, the maximum perturbation height dramatically increases with increasing boundary layer potential temperature (Figure 11d). The similar responses from the maximum updraft and the maximum cloud top over the deep regime imply that stronger updraft accomplishes the maximum aerosol venting, a result that is to be expected.

Over the shallow regime, the variance-based sensitivity analysis reveals that two parameters explain approximately 60% of the output variance: boundary layer potential temperature (31%) and inversion layer strength (29%). A warmer boundary layer and a weaker inversion layer lead to higher maximum perturbation heights (Figures 13e and 13f). These two parameters, which impact the lower tropospheric convective instability, are the same parameters that are key to the maximum updraft speed in the shallow regime. However, the relative importance of the boundary layer potential temperature here is similar to that of the inversion layer strength. It appears that the warmer and unstable boundary layer air that encounters the sea breeze-initiated convective updraft becomes more buoyant, ascends to a higher location, and transports the tracers to a higher height.

In IvJ18, soil saturation fraction is found to be the controlling parameter for the maximum location of the positive aerosol perturbation (45%) in an arid regime. In the moist regime examined here, sea breeze frontal uplift and boundary layer mixing are the primary processes responsible for the vertical redistribution of the tracers. In the presence of vigorous moist sea breeze-initiated convection, convective updrafts transport the tracer further aloft than the frontal uplift alone. Therefore, parameters contributing to the updraft strength variability also contribute to the variability in the vertical redistribution of tracer concentrations.

4. Summary and Discussion

In this study, the relative importance of 10 different environmental parameters to the following characteristics of simulated tropical sea breeze convection is assessed: (1) the inland extent and characteristics of the sea breeze, (2) the intensity of convective updrafts over the land, and (3) the vertical redistribution of aerosols. Six atmospheric and four surface parameters, which describe the initial conditions of idealized sea breeze simulations, are perturbed simultaneously. A perturbed parameter ensemble of 130 sea breeze simulations is carried out using a high-resolution cloud-resolving model coupled to a two-way interactive land-surface model. Using statistical emulators, we conduct variance-based sensitivity analysis on each model output, thus decomposing the model output variance into contributions from the individual parameters and their interactions. This study builds upon IvJ18, which is the first study in the literature to examine the

multidimensional sensitivity of the sea breeze characteristics and associated aerosol transport in a dry coastal desert environment.

In contrast to IvJ18, the current study considers moist convective processes and the role of interactive vegetation. The maximum inland extent of the sea breeze is mainly controlled by initial wind speed in both dry and moist regimes. In both regimes, the soil saturation fraction is found to be the predominant parameter for the sea breeze acceleration followed by the initial wind speed. Unlike the dry environment, the inversion layer strength and boundary layer height are identified to be significant for the sea breeze acceleration in the moist environment, possibly due to the susceptibility of sea breeze to the entrainment and turbulence of the ambient flow.

Our results also show that the mixed layer depth after the passage of the sea breeze is influenced by boundary layer height, initial wind speed, inversion layer strength, soil saturation fraction, and the sea-air temperature difference. Only boundary layer height, inversion layer strength, and sea-air temperature difference were important for the sea breeze mixed layer depth in the dry environment. The two additional parameters found to be important in the moist environment are (1) the soil saturation fraction, which influences the formation of convective clouds over land that then affect the boundary layer development and surface flux partitioning, and (2) the initial wind speed, which interacts with the vegetation canopy and influences the boundary layer turbulence.

The most vigorous convection, and the accompanying deepest clouds and strong updrafts, are localized along the sea breeze. In our ensemble we find two distinct regimes of this sea breeze-initiated convection: a shallow and a deep convection regime. Over the shallow regime, where the CAPE is limited, the initial inversion layer strength and boundary layer temperature are revealed as the main contributors to the intensity of the updraft speed, since they modulate the convective instability in the lower troposphere. In the deep regime, the primary control of the updraft speed is the initial boundary layer potential temperature, which is also a primary driver of the CAPE.

Ahead of the sea breeze, diurnal boundary layer convection develops. While the daytime boundary layer convection and accompanying weaker updrafts are not initiated by sea breeze forcing, they could play a substantial role in the preconditioning of the sea breeze convection. The boundary layer convection updraft speeds increase when boundary layer mixing is active due to drier soil or a weaker inversion.

To assess environmental parameters contributing to the variability in the potential vertical redistribution of the aerosol via convection, the change in the number concentration of the microphysically and radiatively inactive tracers between sunrise and sunset is examined. Whereas the aerosol venting is associated primarily with the frontal lift and the boundary layer mixing behind the sea breeze front in the dry regime, in this study of the moist environments, aerosols are vented higher aloft in the presence of the moist deep convective processes initiated along the sea breeze.

The results of this study also have the following implications for the improvement of operational weather and air quality forecasting in the sea breeze regime:

1. While the initial wind speed is found to be critical for coastal zones with both bare soil desert and tropical rainforests, different surface characteristics (e.g., vegetation canopy, surface roughness length, soil type) can significantly impact the wind flow via surface fluxes and associated turbulence, thereby altering the sea breeze structure. The impact of surface characteristics on the sea breeze can be further convoluted over coastal urban regions with urban heat island and complex building geometry (Hu & Xue, 2016). Therefore, further sensitivity experiments of the sea breeze over coastal urban regions could be particularly beneficial for coastal megacities (e.g., Luanda, Panama, Kuala Lumpur). In summary, better representation of the near-surface wind fields (which current numerical weather prediction struggles with; e.g., Crook & Sun, 2004; Hong, 2003; Spark & Connor, 2004), and utilization of an interactive land-surface (e.g., Holtslag et al., 2013), are possible avenues for improving sea breeze forecasts.
2. Warmer boundary layer potential temperature leading to higher CAPE produces deep convection along the sea breeze whereas inversion layer strength has more of an impact on whether the convection remains primarily shallow. This result highlights the need to better represent convective instability of both near-surface and the entire tropospheric column if we are to predict coastal convection and

resulting aerosol transport properly. In order to do this, attention should be given to improving both our representation of environmental specific humidity as well as surface processes.

3. Significant parameter interactions are found to be important to the maximum updraft in the shallow regime. This underscores the importance of further investigating the interactions between the environmental parameters that control the intensity of the sea breeze-initiated convection.

This study identifies the key parameters impacting tropical sea breeze and associated convective activities, and subsequently hints which properties warrant further investigation. To enhance the process-level understanding, future studies can build on this study focusing on the feedback mechanisms involving aerosol-cloud-land surface interactions.

Acknowledgments
This work was supported by the Office of Naval Research project entitled "Advancing Littoral Zone Aerosol Prediction via Holistic Studies in Regime-Dependent Flows" under grant N00014–16–1-2040. J. S. Johnson was supported by the UK-China Research & Innovation Partnership Fund through the Met Office Climate Science for Service Partnership (CSSP) China as part of the Newton Fund and by the Natural Environment Research Council ACIDPRUF project (grant NE/I020059/1). The RAMS simulations were performed at the Navy Department of Defense Supercomputing Resource Center, and the source code and name list used to generate output data have been archived indefinitely in the Colorado State University Digital Repository (https://hdl.handle.net/10217/199723).

References

Arritt, R. W. (1993). Effects of the large-scale flow on characteristics features of the sea breeze. *Journal of Applied Meteorology*, *32*(1), 116–125. https://doi.org/10.1175/1520-0450(1993)032<0116:EOTLSF>2.0.CO;2

Atkins, N. T., Wakimoto, R. M., & Weckwerth, T. M. (1995). Observations of the sea breeze front during CaPE. Part II: Dual-Doppler and Aircraft Analysis. *Monthly Weather Review*, *123*, 944–969. https://doi.org/10.1175/1520-0493(1995)123<0944:OOTSBF>2.0.CO;2

Baker, R. D., Lynn, B. H., Boone, A., Tao, W. K., & Simpson, J. (2001). The influence of soil moisture, coastline curvature, and land-breeze circulations on sea-breeze-initiated precipitation. *Journal of Hydrometeorology*, *2*(2), 193–211. https://doi.org/10.1175/1525-7541(2001)002<0193:TIOSMC>2.0.CO;2

Banta, R. M., Olivier, L. D., & Levinson, D. H. (1993). Evolution of the Monterey Bay sea-breeze layer as observed by pulsed Doppler lidar. *Journal of the Atmospheric Sciences*, *50*(24), 3959–3982. https://doi.org/10.1175/1520-0469(1993)050<3959:EOTMBS>2.0.CO;2

Banta, R. M., Senff, C. J., Alvarez, R. J., Langford, A. O., Parrish, D. D., Trainer, M. K., et al. (2011). Dependence of daily peak O3 concentrations near Houston, Texas on environmental factors: Wind speed, temperature, and boundary-layer depth. *Atmospheric Environment*, *45*(1), 162–173. https://doi.org/10.1016/j.atmosenv.2010.09.030

Blumenthal, D. L., White, W. H., & Smith, T. B. (1978). Anatomy of a Los Angeles smog episode: Pollutant transport in the daytime sea breeze regime. *Atmospheric Environment (1967)*, *12*(4), 893–907. https://doi.org/10.1016/0004-6981(78)90028-8

Boybeyi, Z., & Raman, S. (1992). A three-dimensional numerical sensitivity study of convection over the Florida peninsula. *Boundary-Layer Meteorology*, *60*(4), 325–359. https://doi.org/10.1007/BF00155201

Caicedo, V., Rappenglueck, B., Cuchiara, G., Flynn, J., Ferrare, R., Scarino, A. J., et al. (2019). Bay breeze and sea breeze circulation impacts on the planetary boundary layer and air quality from an observed and modeled DISCOVER-AQ Texas case study. *Journal of Geophysical Research: Atmospheres*, *124*, 7359–7378. https://doi.org/10.1029/2019JD030523

Clarke, R. H. (1983). Fair weather nocturnal inland wind surges and atmospheric bores: Part I nocturnal wind surges. *Australian Meteorological Magazine*, *31*, 133–145.

Cotton, W. R., Alexander, G. D., Hertenstein, R., Walko, R. L., McAnelly, R. L., & Nicholls, M. (1995). Cloud venting—A review and some new global annual estimates. *Earth-Science Reviews*, *39*(3-4), 169–206. https://doi.org/10.1016/0012-8252(95)00007-0

Cotton, W. R., Pielke, R. A., Walko, R. L., Liston, G. E., Tremback, C. J., Jiang, H., et al. (2003). RAMS 2001: Current status and future directions. *Meteorology and Atmospheric Physics*, *82*(1-4), 5–29. https://doi.org/10.1007/s00703-001-0584-9

Crook, N. A., & Sun, J. (2004). Analysis and forecasting of the low-level wind during the Sydney 2000 Forecast Demonstration Project. *Weather and Forecasting*, *19*(1), 151–167. https://doi.org/10.1175/1520-0434(2004)019<0151:AAFOTL>2.0.CO;2

Crosman, E. T., & Horel, J. D. (2010). Sea and lake breezes: A review of numerical studies. *Boundary-Layer Meteorology*, *137*(1), 1–29. https://doi.org/10.1007/s10546-010-9517-9

Darby, L. S., Banta, R. M., & Pielke, R. A. Sr. (2002). Comparisons between mesoscale model terrain sensitivity studies and Doppler lidar measurements of the sea breeze at Monterey Bay. *Monthly Weather Review*, *130*(12), 2813–2838. https://doi.org/10.1175/1520-0493(2002)130<2813:CBMMTS>2.0.CO;2

Ding, A., Wang, T., Zhao, M., Wang, T., & Li, Z. (2004). Simulation of sea-land breezes and a discussion of their implications on the transport of air pollution during a multi-day ozone episode in the Pearl River Delta of China. *Atmospheric Environment*, *38*(39), 6737–6750. https://doi.org/10.1016/j.atmosenv.2004.09.017

Doswell, C. A. (2001). Severe convective storms—An overview. In C. A. Doswell (Ed.), *Severe Convective Storms*, *Meteorological Monographs* (Vol. 28, pp. 1–26). Boston: American Meteorological Society.

Drobinski, P., Rotunno, R., & Dubos, T. (2011). Linear theory of the sea breeze in a thermal wind. *Quarterly Journal of the Royal Meteorological Society*, *137*(659), 1602–1609. https://doi.org/10.1002/qj.847

Edinger, J. G., & Helvey, R. A. (1961). The San Fernando convergence zone. *Bulletin of the American Meteorological Society*, *42*(9), 626–637. https://doi.org/10.1175/1520-0477-42.9.626

Emanuel, K. A. (1994). *Atmospheric Convection*. New York: Oxford University Press.

Estoque, M. A. (1962). The sea breeze as a function of the prevailing synoptic situation. *Journal of the Atmospheric Sciences*, *19*(3), 244–250. https://doi.org/10.1175/1520-0469(1962)019<0244:TSBAAF>2.0.CO;2

Fankhauser, J. C., Crook, N. A., Tuttle, J., Miller, L. J., & Wade, C. G. (1995). Initiation of deep convection along boundary layer convergence lines in a semitropical environment. *Monthly Weather Review*, *123*(2), 291–314. https://doi.org/10.1175/1520-0493(1995)123<0291:IODCAB>2.0.CO;2

Finkele, K. (1998). Inland and offshore propagation speeds of a sea breeze from simulations and measurements. *Boundary-Layer Meteorology*, *87*(2), 307–329. https://doi.org/10.1023/a:1001083913327

Fovell, R. (2005). Convective initiation ahead of the sea-breeze front. *Monthly Weather Review*, *133*(1), 264–278. https://doi.org/10.1175/MWR-2852.1

Freitas, E. D., Rozoff, C. M., Cotton, W. R., & Silva Dias, P. L. (2006). Interactions of an urban heat island and sea-breeze circulations during winter over the metropolitan area of São Paulo, Brazil. *Boundary-Layer Meteorology*, *122*(1), 43–65. https://doi.org/10.1007/s10546-006-9091-3

Grant, L. D., & van den Heever, S. C. (2014). Aerosol-cloud-land surface interactions within tropical sea breeze convection. *Journal of Geophysical Research: Atmospheres*, *119*, 8340–8361. https://doi.org/10.1002/2014JD021912

Harrington, J. Y. (1997). The effects of radiative and microphysical processes on simulated warm and transition season Arctic stratus (Doctoral dissertation). Fort Collins, CO: Colorado State University.
Holtslag, A. A. M., Svensson, G., Baas, P., Basu, S., Beare, B., Beljaars, A. C. M., et al. (2013). Stable atmospheric boundary layers and diurnal cycles: Challenges for weather and climate models. *Bulletin of the American Meteorological Society*, *94*(11), 1691–1706. https://doi.org/10.1175/BAMS-D-11-00187.1
Hong, J. S. (2003). Evaluation of the high-resolution model forecasts over the Taiwan area during GIMEX. *Weather and Forecasting*, *18*(5), 836–846. https://doi.org/10.1175/1520-0434(2003)018<0836:EOTHMF>2.0.CO;2
Hu, X. M., & Xue, M. (2016). Influence of synoptic sea-breeze fronts on the urban heat island intensity in Dallas–Fort Worth, Texas. *Monthly Weather Review*, *144*(4), 1487–1507. https://doi.org/10.1175/MWR-D-15-0201.1
Igel, A. L., van den Heever, S. C., & Johnson, J. S. (2018). Meteorological and land surface properties impacting sea breeze extent and aerosol distribution in a dry environment. *Journal of Geophysical Research: Atmospheres*, *123*, 22–37. https://doi.org/10.1002/2017JD027339
Iwai, H., Murayama, Y., Ishii, S., Mizutani, K., Ohno, Y., & Hashiguchi, T. (2011). Strong updraft at a sea-breeze front and associated vertical transport of near-surface dense aerosol observed by doppler lidar and ceilometer. *Boundary-Layer Meteorology*, *141*(1), 117–142. https://doi.org/10.1007/s10546-011-9635-z
Johnson, J. S., Cui, Z., Lee, L. A., Gosling, J. P., Blyth, A. M., & Carslaw, K. S. (2015). Evaluating uncertainty in convective cloud microphysics using statistical emulation. *Journal of Advances in Modeling Earth Systems*, *7*, 162–187. https://doi.org/10.1002/2014MS000383
Kala, J., Lyons, T. J., Abbs, D. J., & Nair, U. S. (2010). Numerical simulations of the impacts of land-cover change on a southern sea breeze in south-west Western Australia. *Boundary-Layer Meteorology*, *135*(3), 485–503. https://doi.org/10.1007/s10546-010-9486-z
Kingsmill, D. E. (1995). Convection initiation associated with a sea-breeze front, a gust front, and their collision. *Monthly Weather Review*, *123*(10), 2913–2933. https://doi.org/10.1175/1520-0493(1995)123<2913:CIAWAS>2.0.CO;2
Lee, L. A., Carslaw, K. S., Pringle, K. J., Mann, G. W., & Spracklen, D. V. (2011). Emulation of a complex global aerosol model to quantify sensitivity to uncertain parameters. *Atmospheric Chemistry and Physics*, *11*(23), 12,253–12,273. https://doi.org/10.5194.acp-11-12253-2011
Lee, L. A., Pringle, K. J., Reddington, C. L., Mann, G. W., Stier, P., Spracklen, D. V., et al. (2013). The magnitude and causes of uncertainty in global model simulations of cloud condensation nuclei. *Atmospheric Chemistry and Physics*, *13*(17), 8879–8914. https://doi.org/10.5194/acp-13-8879-2013
Liu, H., Chan, J. C., & Cheng, A. Y. (2001). Internal boundary layer structure under sea-breeze conditions in Hong Kong. *Atmospheric Environment*, *35*(4), 683–692. https://doi.org/10.1016/S1352-2310(00)00335-6
Lombardo, K., Sinsky, E., Edson, J., Whitney, M. M., & Jia, Y. (2018). Sensitivity of offshore surface fluxes and sea breezes to the spatial distribution of sea-surface temperature. *Boundary-Layer Meteorology*, *166*(3), 475–502. https://doi.org/10.1007/s10546-017-0313-7
Loughner, C. P., Tzortziou, M., Follette-Cook, M., Pickering, K. E., Goldberg, D., Satam, C., et al. (2014). Impact of bay-breeze circulations on surface air quality and boundary layer export. *Journal of Applied Meteorology and Climatology*, *53*(7), 1697–1713. https://doi.org/10.1175/JAMC-D-13-0323.1
Lu, R., & Turco, R. P. (1994). Air pollutant transport in a coastal environment. Part I: Two-dimensional simulations of sea-breeze and mountain effects. *Journal of the Atmospheric Sciences*, *51*(15), 2285–2308. https://doi.org/10.1175/1520-0469(1994)051<2285:APTIAC>2.0.CO;2
Lyons, W. A., Pielke, R. A., Tremback, C. J., Walko, R. L., Moon, D. A., & Keen, C. S. (1995). Modeling impacts of mesoscale vertical motions upon coastal zone air pollution dispersion. *Atmospheric Environment*, *29*(2), 283–301. https://doi.org/10.1016/1352-2310(94)00217-9
Melas, D., & Kambezidis, H. D. (1992). The depth of the internal boundary layer over an urban area under sea-breeze conditions. *Boundary-Layer Meteorology*, *61*(3), 247–264. https://doi.org/10.1007/BF02042934
Meyers, M. P., Walko, R. L., Harrington, J. Y., & Cotton, W. R. (1997). New RAMS cloud microphysics parameterization. Part II: The two-moment scheme. *Atmospheric Research*, *45*(1), 3–39. https://doi.org/10.1016/S0169-8095(97)00018-5
Miao, J. F., Kroon, L. J. M., de Arellano, J. V. G., & Holtslag, A. A. M. (2003). Impacts of topography and land degradation on the sea breeze over eastern Spain. *Meteorology and Atmospheric Physics*, *84*(3-4), 157–170. https://doi.org/10.1007/s00703-002-0579-1
Miller, S. T., & Keim, B. D. (2003). Synoptic-scale controls on the sea breeze of the central New England coast. *Weather and Forecasting*, *18*(2), 236–248. https://doi.org/10.1175/1520-0434(2003)018<0236:SCOTSB>2.0.CO;2
Miller, S. T. K., Keim, B. D., Talbot, R. W., & Mao, H. (2003). Sea breeze: Structure, forecasting, and impacts. *Reviews of Geophysics*, *41*(3), 1011. https://doi.org/10.1029/2003RG000124
Moncrieff, M. W., & Liu, C. (1999). Convection initiation by density currents: Role of convergence, shear, and dynamical organization. *Monthly Weather Review*, *127*(10), 2455–2464. https://doi.org/10.1175/1520-0493(1999)127<2455:CIBDCR>2.0.CO;2
Morris, M. D., & Mitchell, T. J. (1995). Exploratory designs for computational experiments. *Journal of Statistical Planning and Inference*, *43*(3), 381–402. https://doi.org/10.1016/0378-3758(94)00035-T
Muppa, S. K., Anandan, V. K., Kesarkar, K. A., Rao, S. V. B., & Reddy, P. N. (2012). Study on deep inland penetration of sea breeze over complex terrain in the tropics. *Atmospheric Research*, *104*, 209–216. https://doi.org/10.1016/j.atmosres.2011.10.007
Ogawa, S., Sha, W., Iwasaki, T., & Wang, Z. (2003). A numerical study on the interaction of a sea-breeze front with convective cells in the daytime boundary layer. *Journal of the Meteorological Society of Japan*, *81*(4), 635–651. https://doi.org/10.2151/jmsj.81.635
O'Hagan, A. (2006). Bayesian analysis of computer code outputs: A tutorial. *Reliability Engineering & System Safety*, *91*(10-11), 1290–1300. https://doi.org/10.1016/j.ress.2005.11.025
Physick, W. L., & Smith, R. K. (1985). Observations and dynamics of sea-breezes in northern Australia. *Australian Meteorological Magazine*, *33*(2), 51–63.
Porson, A., Steyn, D. G., & Schayes, G. (2007). Formulation of an index for sea breezes in opposing winds. *Journal of Applied Meteorology and Climatology*, *46*(8), 1257–1263.
Pujol, G., Iooss, B., & Janon, A. (2013). Sensitivity: Sensitivity analysis, R package version 1.7.
R Core Team (2017). *R: A language and environment for statistical computing*. Vienna, Austria: R Foundation for Statistical Computing.
Reible, D. D., Simpson, J. E., & Linden, P. F. (1993). The sea breeze and gravity-current frontogenesis. *Quarterly Journal of the Royal Meteorological Society*, *119*(509), 1–16. https://doi.org/10.1002/qj.49711950902
Reynolds, R. W., Smith, T. M., Liu, C., Chelton, D. B., Casey, K. S., & Schlax, M. G. (2007). Daily high-resolution-blended analyses for sea surface temperature. *Journal of Climate*, *20*(22), 5473–5496. https://doi.org/10.1175/2007JCLI1824.1
Rieck, M., Hohenegger, C., & Gentine, P. (2015). The effect of moist convection on thermally induced mesoscale circulations. *Quarterly Journal of the Royal Meteorological Society*, *141*(691), 2418–2428. https://doi.org/10.1002/qj.2532

Rochetin, N., Couvreux, F., & Guichard, F. (2017). Morphology of breeze circulations induced by surface flux heterogeneities and their impact on convection initiation. *Quarterly Journal of the Royal Meteorological Society*, *143*(702), 463–478. https://doi.org/10.1002/qj.2935

Rousseau-Rizzi, R., Kirshbaum, D. J., & Yau, M. K. (2017). Initiation of deep convection over an idealized mesoscale convergence line. *Journal of Atmospheric Science*, *74*(3), 835–853. https://doi.org/10.1175/JAS-D-16-0221.1

Roustant, O., Ginsbourger, D., & Deville, Y. (2012). DiceKriging, DiceOptim: Two R packages for the analysis of computer experiments by kriging-based metamodeling and optimization. *Journal of Statistical Software*, *51*(1), 1–55.

Saleeby, S. M., & Cotton, W. R. (2004). A large-droplet mode and prognostic number concentration of cloud droplets in the Colorado State University Regional Atmospheric Modeling System (RAMS). Part I: Module descriptions and supercell test simulations. *Journal of Applied Meteorology*, *43*(1), 182–195. https://doi.org/10.1175/1520-0450(2004)043<0182:ALMAPN>2.0.CO;2

Saleeby, S. M., & van den Heever, S. C. (2013). Developments in the CSU-RAMS aerosol model: Emissions, nucleation, regeneration, deposition, and radiation. *Journal of Applied Meteorology and Climatology*, *52*(12), 2601–2622. https://doi.org/10.1175/jamc-d-12-0312.1

Saltelli, A., Chan, K., & Scott, E. M. (2000). *Sensitivity Analysis*. New York: John Wiley.

Saltelli, A., Tarantola, S., & Chan, K. S. (1999). A quantitative model-independent method for global sensitivity analysis of model output. *Technometrics*, *41*(1), 39–56. https://doi.org/10.1080/00401706.1999.10485594

Seroka, G., Fredj, E., Khout, J., Dunk, R., Miles, T., & Glenn, S. (2018). Sea breeze sensitivity to coastal upwelling and synoptic flow using Lagrangian methods. *Journal of Geophysical Research: Atmospheres*, *123*, 9443–9461. https://doi.org/10.1029/2018JD028940

Simpson, J. E. (1994). *Sea breeze and local winds*. Cambridge: Cambridge University Press.

Simpson, J. E., Mansfield, D. A., & Milford, J. R. (1977). Inland penetration of sea-breeze fronts. *Quarterly Journal of the Royal Meteorological Society*, *103*(435), 47–76. https://doi.org/10.1002/qj.49710343504

Soderholm, J., McGowan, H., Richter, H., Walsh, K., Weckwerth, T., & Coleman, M. (2016). The Coastal Convective Interactions Experiment (CCIE): Understanding the role of sea breezes for hailstorm hotspots in eastern Australia. *Bulletin of the American Meteorological Society*, *97*(9), 1687–1698. https://doi.org/10.1175/BAMS-D-14-00212.1

Spark, E., & Connor, G. J. (2004). Wind forecasting for the sailing events at the Sydney 2000 Olympic and Paralympic Games. *Weather and Forecasting*, *19*(2), 181–199. https://doi.org/10.1175/1520-0434(2004)019<0181:WFFTSE>2.0.CO;2

Stein, U., & Alpert, P. (1993). Factor separation in numerical simulations. *Journal of the Atmospheric Sciences*, *50*(14), 2107–2115. https://doi.org/10.1175/1520-0469(1993)050<2107:FSINS>2.0.CO;2

Thompson, W. T., Holt, T., & Pullen, J. (2007). Investigation of a sea breeze front in an urban environment. *Quarterly Journal of the Royal Meteorological Society*, *133*(624), 579–594. https://doi.org/10.1002/qj.52

Tijm, A. B. C., Van Delden, A. J., & Holtslag, A. A. M. (1999). The inland penetration of sea breezes. *Contributions to Atmospheric Physics*, *72*(4), 317–328.

Verma, S., Boucher, O., Venkataraman, C., Reddy, M. S., Müller, D., Chazette, P., & Crouzille, B. (2006). Aerosol lofting from sea breeze during the Indian Ocean Experiment. *Journal of Geophysical Research*, *111*, 07208. https://doi.org/10.1029/2005JD005953

Verma, S., Pani, S. K., Kumar, D. B., Faruqi, A. R., Bhanja, S. N., & Mandal, M. (2016). Aerosol extinction properties over coastal West Bengal Gangetic plain under inter-seasonal and sea breeze influenced transport processes. *Atmospheric Research*, *167*, 224–236. https://doi.org/10.1016/j.atmosres.2015.07.021

Waite, M. L., & Khouider, B. (2010). The deepening of tropical convection by congestus preconditioning. *Journal of the Atmospheric Sciences*, *67*(8), 2601–2615. https://doi.org/10.1175/2010JAS3357.1

Walko, R. L., Band, L. E., Baron, J., Kittel, T. G. F., Lammers, R., Lee, T. J., et al. (2000). Coupled atmosphere–biophysics–hydrology models for environmental modeling. *Journal of Applied Meteorology*, *39*(6), 931–944. https://doi.org/10.1175/1520-0450(2000)039<0931:CABHMF>2.0.CO;2

Walko, R. L., Cotton, W. R., Meyers, M. P., & Harrington, J. Y. (1995). New RAMS cloud microphysics parameterization part I: The single-moment scheme. *Atmospheric Research*, *38*(1-4), 29–62. https://doi.org/10.1016/0169-8095(94)00087-T

Wellmann, C., Barrett, A. I., Johnson, J. S., Kunz, M., Vogel, B., Carslaw, K. S., & Hoose, C. (2018). Using emulators to understand the sensitivity of deep convective clouds and hail to environmental conditions. *Journal of Advances in Modeling Earth Systems*, *10*, 3103–3122. https://doi.org/10.1029/2018MS001465

Wilson, J. W., & Megenhardt, D. L. (1997). Thunderstorm initiation, organization, and lifetime associated with Florida boundary layer convergence lines. *Monthly Weather Review*, *125*(7), 1507–1525. https://doi.org/10.1175/1520-0493(1997)125<1507:TIOALA>2.0.CO;2

Xian, Z., & Pielke, R. A. (1991). The effects of width of landmasses on the development of sea breezes. *Journal of Applied Meteorology*, *30*(9), 1280–1304. https://doi.org/10.1175/1520-0450(1991)030<1280:TEOWOL>2.0.CO;2

Zhong, S., Leone, J. M., & Takle, E. S. (1991). Interaction of the sea breeze with a river breeze in an area of complex coastal heating. *Boundary-Layer Meteorology*, *56*(1-2), 101–139. https://doi.org/10.1007/BF00119964